Utrecht University

Reconstructing oceanographic changes and the evolution of the "cold water route" through glacial-interglacial variability of MIS 12-11 in the Falkland Region, Southern Atlantic Ocean

IODP Site U1534

Thomas Camiel van der Vliet

MSc Thesis Marine Sciences – final version

Supervised by dr. P. K. Bijl[1] & dr. L. Thöle[1]

Department of Earth Sciences, Faculty of Geosciences, Utrecht University

[1]Marine Palynology and Palaeoceanography

July 8th, 2022.

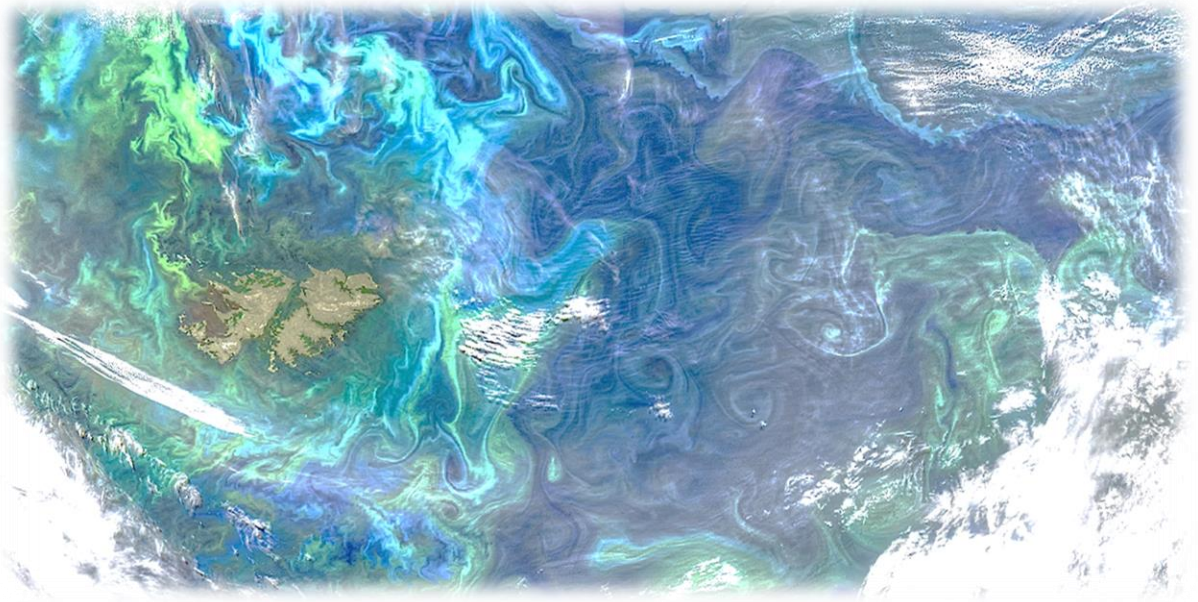

Falkland Islands / *Islas Malvinas*

Modified satellite image; credits: *NASA/Goddard Space Flight Center Ocean Color/NOAA-20/NASA-NOAA Suomi NPP*)

Abstract

Shifts of the Southern Hemisphere Westerly Winds have induced latitudinal migration of Southern Oceanic fronts on glacial-interglacial timescales. It is indicated that such frontal migrations in the Drake Passage region, particularly of the Subantarctic Front, significantly alter the flow of the Antarctic Circumpolar Current through the Drake Passage, which impacts the exchange of Pacific-sourced cold water into the South Atlantic, referred to as the "cold water route". This study focuses on the interval covering the warm interglacial Marine Isotope Stage 11 (474 – 424 ka) and the preceding glacial maximal Marine Isotope Stage 12 to give insight into the nature of oceanographic changes during and towards previous warm climate interval. International Ocean Discovery Program Site U1534 is situated in the vicinity of the Subantarctic Front, on the South Falkland Slope Drift north-east to the Drake Passage. The site is therefore ideally located to identify changes in the Subantarctic Front and the cold water route. Organic proxies for the reconstruction of surface oceanographic conditions were used, notably organic-walled dinoflagellate cyst paleo-assemblages and biomarker proxy TEX_{86} for sea surface temperature reconstruction. The dinoflagellate cyst assemblage reflects a notable change from glacial to interglacial conditions, although the latter indicates influence from a warmer environment, likely from the Patagonian shelf water, as wel from colder and dynamic waters related to the Subantarctic Front. However, the TEX_{86}-based sea surface temperature reconstruction is mirrored to the general warming of MIS 11 It displays a cooling trend from ~13°C to 6-8°C during the transition into MIS 11 and remains stable throughout most of the interglacial, which is suggested to reflects the enhanced transport of the cold water via the Subantarctic Front into the Southwest Atlantic Ocean. However, a dimmed transport of the cold water into the region is suspected as the sea surface temperature suddenly rose at the later stage of MIS 11, ca. 30,000 years after global warming of Termination V. This study therefore concludes that the cold water route resulted in a subdued and delayed effect of interglacial warming in the Falkland Region.

Keywords: marine palynology, organic geochemistry, dinoflagellates, Mid-Pleistocene, MIS 11, Termination V, glacial-interglacial variability, Atlantic Circumpolar Current, Subantarctic Front, the cold water route, Falkland Plateau, Southern Ocean, IOPD Expedition 382 Site U1534.

Table of Contents

Table of Figures

1. Introduction

The Southern Ocean modulates atmospheric CO_2 levels on glacial-interglacial timescales due to its prevalence in the communication between the atmosphere, surface waters, and the deep ocean carbon reservoir (Burke & Robinson, 2012). It is estimated that the Southern Ocean has been responsible for the uptake of 40% of the global anthropogenic CO_2 over the last 150 years (Gruber et al., 2018; Ito et al., 2010; Sabine et al., 2004) and for even a larger portion of excess heat uptake (Armour et al., 2016; Shi et al., 2018). The driving mechanisms of carbon and heat exchange are closely related to sea ice expansion, aeolian iron-bearing dust supply, subantarctic phytoplankton productivity (Ferrari et al., 2014; Jaccard et al., 2012; Kohfeld & Chase, 2017; Toyos et al., 2022). Such mechanisms were found to be enhanced during glacial phases, while the exchange of surface waters with the deep ocean carbon reservoir in the Antarctic Zone appeared to be weaker (Marshall & Speer, 2012; Williams et al., 2019) Glacial phases were therefore expected to have had a diminishing effect on atmospheric CO_2 levels (Sigman et al., 2010).

Contradictory, interglacial phases were subjected to enhanced outgassing of CO_2 from the Southern Ocean surface waters, mainly due to enhanced upwelling that promotes transport of abyssal carbon to the surface ocean (Sigman et al., 2010). Upwelling occurs predominantly along fronts of the Antarctic Circumpolar Current (ACC) (Armour et al., 2016) and is thought to be modulated by changes in strength and/or the position of Southern Hemisphere Westerlies (SWW) on glacial-interglacial timescales (Ai et al., 2020; Anderson et al., 2009; Toggweiler, 2009).

In this thesis, one of the strongest transitions from glacial to interglacial conditions in the geological past is investigated, namely the transition from Marine Isotope Stage (MIS) 12 to MIS 11 (ca. 440 to 400 thousand years ago (ka) (Candy et al., 2014)). The latter is considered an analogue for near-future anthropogenic warming due to its exceptional warming pattern compared to other Pleistocene interglacials (Droxler & Howard, 2003). Studying significant previous warm intervals and the transition towards it can provide insights into how Southern Ocean carbon and heat exchange will evolve regarding the ongoing anthropogenic climate change (Gruber et al., 2018; Le Quéré et al., 2007).

Palaeoceanographic reconstructions generally agree that ACC-fronts migrated quasi-latitudinally on glacial-interglacial timescales (Bard & Rickaby, 2009) but find disputes about the strength and temporal patterns of these shifts (Mazaud et al., 2010), especially in complex areas such as the Drake Passage between South America and the Antarctic Peninsula (Rühs et al., 2019). Here, the ACC is constricted to major bathymetric obstructions, making it particularly sensitive to climatic changes and frontal migrations (Lamy et al., 2015; Pérez et al., 2021; Rühs et al., 2019; Smith et al., 2010).

This thesis aims to reconstruct the nature of palaeoceanographic change during the prominent transition of MIS 12-11 at the critical area of the Drake Passage. It thereby contributes to better understand changes in the position and strength of the ACC, and their timing, which can help to identify potential climatic feedback loops, as they have often not been included in projections of future climate change (McClymont et al., 2016; Voigt et al., 2016).

In order to understand the oceanographic changes, following research questions are addressed: how did the surface water evolve during the glacial-interglacial transition of MIS 12 into 11? How sensitive was the sea surface temperature to climate change on glacial-interglacial timescale? How could the changes in surface water be associated with the ACC and with oceanographic changes in the Drake Passage region?

An effective approach to answer these questions rests on the combination of palynological and organic geochemical proxies that are well-suitable for reconstructing past oceanographic conditions at high latitudes. The distribution of organic-walled microfossil remains of near-surface-dwelling dinoflagellates (dinocysts) has shown a strong affinity to specific environmental conditions such as sea surface temperature, salinity, shoreline proximity, and water mass (Harland & Pudsey, 1999). Palaeoceanographic reconstructions are based on the comparison of paleo-assemblages to the modern biogeographic distributions of dinocysts in surface sediments (Esper & Zonneveld, 2007; Marret & Zonneveld, 2003) has increasingly been applied during the last decades (Bijl et al., 2011, 2021; Hartman et al., 2021; Hoem et al., 2021; Howe et al., 1997; G. Williams et al., 2004), and since more recently, specifically for past southern high-latitude conditions (Prebble et al., 2013; Marret et al., 2019; Thöle et al., in prep).

Sediments that bear organic-walled dinocysts are also well-applicable for organic biomarker compounds owing to the similar required preservation conditions as regularly provided at

higher latitudes. The use of biomarkers is a relatively new organic geochemical tool to uncover temperature-based palaeoceanographic evidence. Hence, the TEX_{86} biomarker proxy is applied to reconstruct sea surface temperatures (SST; Schouten et al., 2002; Schouten et al., 2013; Kim et al., 2010; O'Brien et al., 2017).

The combination of proxies is applied on the sedimentary Core U1534 from the International Ocean Discovery Program (IODP) Expedition 382. The core originates from the South Falkland Slope Drift, situated beneath the Subantarctic Front, located to the east of the Drake Passage in the Atlantic sector of the Southern Ocean (Weber et al., 2021). The goal to unravel the palaeoceanography in this region during the prominent transition from MIS 12-11 thus rests on an integrative, multi-proxy approach using biomarker- and dinocyst-based reconstructions of past surface water conditions at Site U1534.

In doing so, this thesis first provides an overview of MIS 12-11 and of the modern regional oceanographic setting, followed by the description of lithology, depositional setting, and age model of the Core U1534. The applied methods based on biomarker and dinocyst assemblages are elaborated, and ultimately, an integrated picture is portrayed of the regional oceanography during MIS 12-11.

1.1 Marine Isotope Stages 12-11

The warm climate interval MIS 11 occurred during the mid-Pleistocene from 424 to 374 ka (Candy et al., 2014; Toyos et al., 2022b). Within the warm interval was a unique interglacial substage, referred to as MIS 11c, centred around 405 ka (Fig. 1; Candy et al., 2014). MIS 11c has

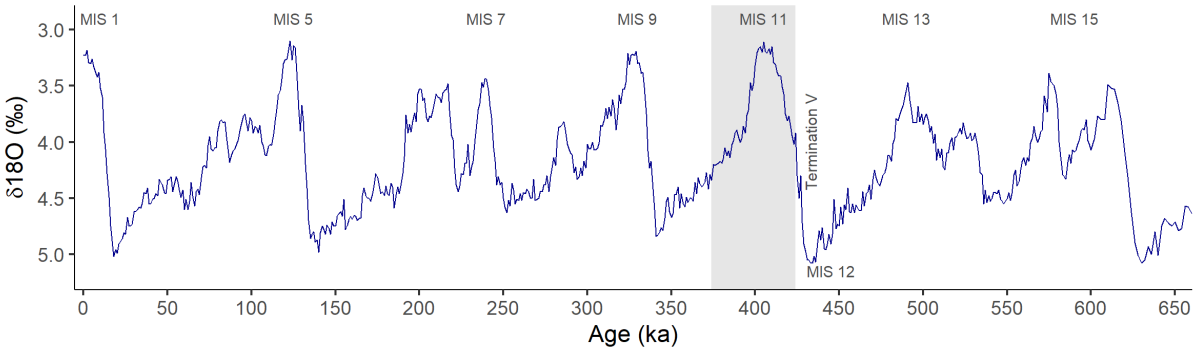

Figure 1. Globally averaged benthic oxygen isotope (δ18O) curve, LR04 (Lisiecki & Raymo, 2005). Warm stages are indicated by MIS 1, 5, 7, 9, 11, 13 and 15. MIS 11 is highlighted in grey.

widely been reviewed as one of the Pleistocene interglacials best suitable analogies for modern global average temperature (Candy et al., 2014; Droxler & Howard, 2003).

The insolation patterns during MIS 11 resemble that of the Holocene most of all interglacials in the past 500 thousand years (kyr) (Candy et al., 2014; Hodell et al., 2000). Because insolation patterns control the duration, structure, and degree of warmth during an interglacial, MIS 11 is suggested as the most appropriate climate analogy for the Holocene (Hodell et al., 2000; Saavedra-Pellitero et al., 2017). MIS 11 is characterized by low eccentricity which led to modest precession-driven insolation changes. It resulted in the interglacial MIS11c, a unique prolonged warm period (ca. 30 kyr) of relatively stable insolation values without a major effect of precession (Candy et al., 2014; Droxler & Howard, 2003).

The transition between MIS 12 and MIS 11, referred to as Termination V (Fig. 1), is unique regarding duration and magnitude. It is the longest glacial termination of the past 500 ka and has the strongest decrease in benthic $\delta^{18}O$ of all Terminations (Candy et al., 2014; Droxler & Howard, 2003; Lisiecki & Raymo, 2005). This requires a strong decrease in the global ice volume, mostly from the Northern Hemisphere. Still, the stability of the West Antarctic Ice Sheet during Termination V and MIS 11 forms an ongoing point of discussion (Hartman et al., 2021; Saavedra-Pellitero et al., 2017).

1.2 The Antarctic Circumpolar Current

The ACC is the world's largest current system, transporting on average ~134 Sv (Smith et al., 2009) in a clockwise direction around Antarctica (Mazaud et al., 2010; Toyos et al., 2022). It thereby effectively isolates cold Antarctic waters from the warmer subtropical waters of the Pacific, Indian, and Atlantic oceans, facilitating the stability of Antarctica's ice sheets (Lamy et al., 2015). Surface wind shear stresses from the SWW cause divergent Ekman transport that leads to upwelling of CO_2 and nutrient-rich subsurface waters along tilted subsurfaces of constant density, called isopycnals (Ai et al., 2020). The isopycnals define characteristic fronts along which the ACC reaches the highest flow speed (Wanner et al., 2008). The southern oceanic fronts have a quasi-latitudinal orientation resulting in strong meridional gradients in environmental conditions such as sea surface temperature, salinity, nitrate- and phosphate concentrations (Chapman et al., 2020; Esper & Zonneveld, 2007). From north to south are the Subtropical Front (STF), Subantarctic Front (SAF), Polar Front (PF), Southern ACC front

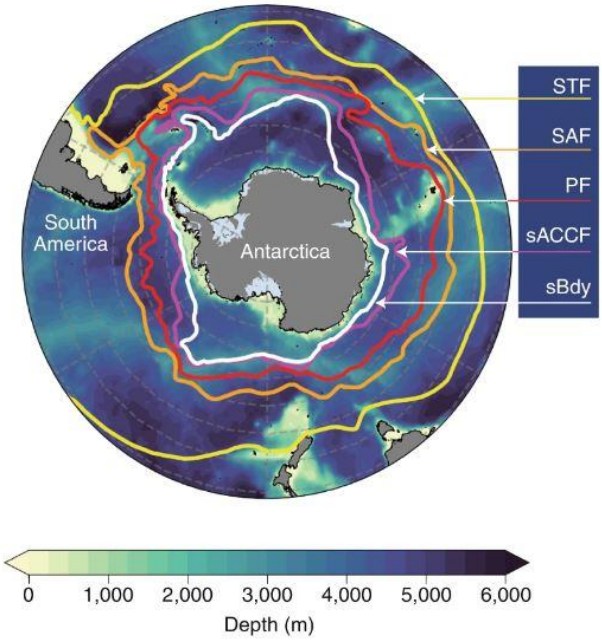

Figure 2. Southern oceanic fronts; North of the Subtropical Front reign the subtropical gyres; the Subantarctic Zone is between the Subtropical Front (STF) and the Subantarctic Front (SAF); Polar Frontal Zone is in proximity of the Polar Front (PF); South of the Polar Front is the Antarctic Zone; where also the southern ACC Front (sACCF) and the Southern Boundary (SBDy) front are located (figure from Chapman et al., 2020).

(sACCF); and the Southern Boundary (SBdy) fronts (Fig. 2; Chapman et al., 2020; Orsi et al., 1995). The fronts act as strong barriers between distinct oceanographic regions or zones with generally stable environmental surface conditions. North of the STF prevail the subtropical gyres with warm (>14°C), nutrient-poor (subtropical) surface water. South of the STF is the Subantarctic Zone (SAZ), with relative cold ($\theta = 8$ °C), nutrient-rich subantarctic surface water associated with high productivity fuelled by aeolian iron-bearing dust supply, while high nutrient concentrations are supplied from the Antarctic Zone. (Toyos et al., 2022b) This zone extends south over the SAF, characterized by 7–9 °C sea surface temperature, until the subantarctic water becomes subducted in the Polar Frontal Zone (PFZ) to form Antarctic Intermediate Water (AAIW; Fig. 3), which sequestrates substantial CO_2 from the atmosphere (Voigt et al., 2016). South of the dynamic PF extends the Antarctic Zone (AZ), characterized by cold (< 0 °C), nutrient-rich but low-productivity (NRLP) signature Antarctic surface water (Williams et al., 2019). The zone, around ~60°, is subjected to large-scale upwelling of high salinity North Atlantic Deep Water (NADW) to just below the sea surface, where it mixes with Antarctic surface water and provides high nutrient concentrations (Hodell et al., 2000). The low productivity in the AZ is mainly due to the deficiency of iron, which is required by autotrophic phytoplankton (Toyos et al., 2022). The area closer to the Antarctic continent

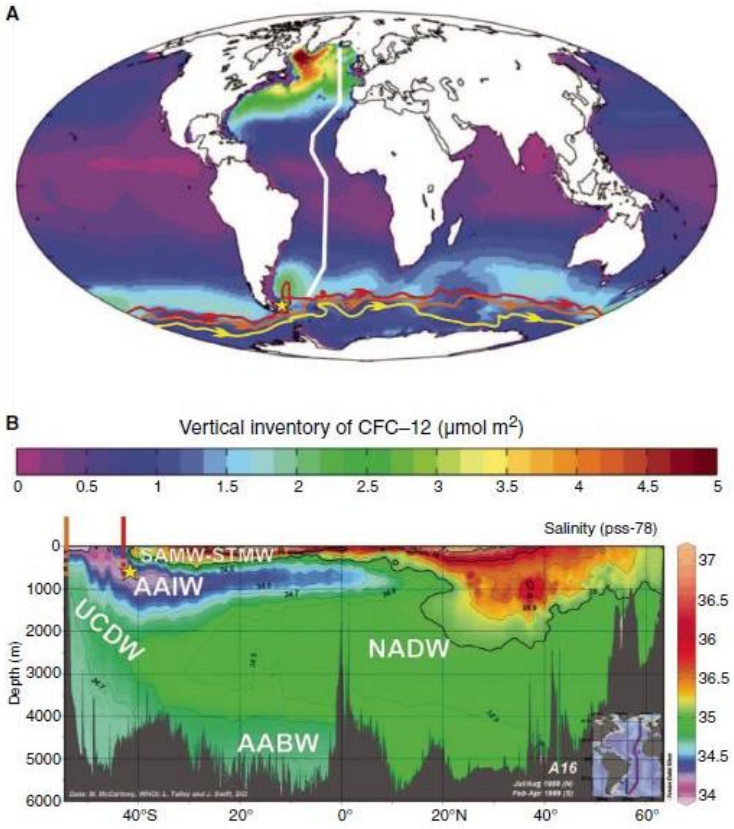

Figure 3. Location of the Subantarctic Front and Antarctic Intermediate Water. Yellow star is the relative hydrographic position of the South Falkland Slope. Top (A): vertically integrated chlorofluorocarbon (CFC)-12 for the present day (1990s), demonstrating the uptake of anthropogenic gases by intermediate water formation in the Subantarctic (Global Ocean Data Analysis Project climatology). red = Subantarctic Front, orange = Polar Front, yellow = southern ACC front (Orsi et al., 1995). Yellow star = South Falkland Slope Drift. Bottom (B): Atlantic meridional vertical salinity profile (white line, above). SAMW = Subantarctic Mode Water, STMW = Subtropical Mode Water, AAIW = Antarctic Intermediate Water, UCDW = Upper Circumpolar Deep Water, NADW = North Atlantic Deep Water, AABW = Antarctic Bottom Water (Figure & description from Weber et al., 2018).

experiences a large extent of winter sea ice coverage. In the proximity of and under the ice happens the formation of Antarctic Bottom Water (AABW), as cold, dense water sinks and extents vastly through the ocean's interior (Orsi et al., 1999; Williams et al., 2019).

1.3 Drake Passage throughflow and the "cold water route

The total ACC transport through the Drake Passage is estimated between ~130 and ~150 Sv (Marshall & Speer, 2012); about one-half of the total transport occurs at and north of the SAF (i.e., in the sub-Antarctic Zone) (Smith et al., 2009; Toyos et al., 2020). In the SE Pacific, the northern extent of the ACC encounters the Chilean west coast, leading to the bifurcation of a ACC to become partly deflected into the northward Humboldt Current System (HCS), while the majority of the ACC is transported southward via the Cape Horn Current (CHC) towards the Drake Passage (Fig. 4; Lamy et al., 2015) and streams along the SAF into the South Atlantic.

The so-called "cold water route" is considered the primary pathway delivering Pacific-sourced cold, dense (sub)Antarctic water into the South Atlantic (Fig. 5; Lamy et al., 2015; Rühs et al., 2019), associated with the transport of AAIW as one of the primary water masses, along with Subantarctic Mode Water (SAMW) on top, and Upper Circumpolar Deep Water UCDW below (Fig. 3; Chapman et al., 2020; Peck et al., 2021; Smith et al., 2010).

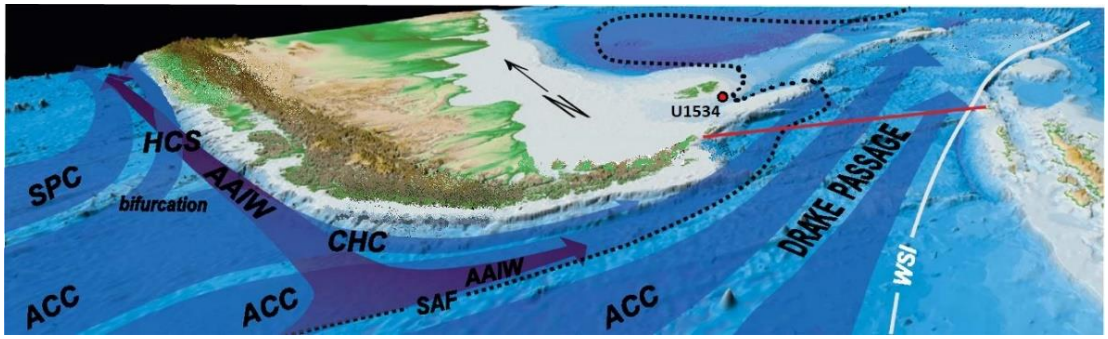

Figure 4. Schematic view of the Drake Passage region oceanography with major surface and intermediate water circulation and currents displayed. IODP Site U1534 is indicated by the yellow dot. AAIW, Antarctic Intermediate Water; HCS, Humboldt Current System; CHC, Cape Horn Current; WSI, winter sea ice; SAF, Subantarctic Front location is approximately based on Orsi et al. (1995); approximate location of Site U1534 is indicated by the red dot (figure modified from Lamy et al., 2015).

Drake Passage throughflow of ACC, and thus the cold water route, is indicated to vary strongly on glacial-interglacial timescales (Lamy et al., 2015). Glacial phases likely experienced a more sluggish northern Drake Passage transport and subsequently a decreased export of Pacific-sourced ACC water into the South Atlantic due to reduced SWW wind shear stresses in the Drake Passage, obstruction of Southern Ocean sea ice, and the enhanced bifurcation of ACC into the equatorward HCS as a result of the northern (at lower latitude) positioned SWW and SAF (Lamy et al., 2015). It is suggested that the southward shift of SWW and fronts, particularly the SAF, significantly reduced the deflection of the ACC into the equatorward HCS and likewise increased ACC transport towards and through the Drake Passage via the CHC. Additionally, wind forcing on the ACC became enhanced due to increased SWW shear stresses southward retreating sea ice. It thereby effectively opened up the "cold water route", resulting in the enhanced transport of sub-Antarctic ACC water into the South Atlantic.

In the Atlantic sector of the Southern Ocean, the ACC proceeds eastwards, mainly via the SAF along the North Scotia Ridge, until Ekman-induced shear stresses cause the majority of the ACC to deflect northward and cross the Ridge through a series of narrow passages into the South Atlantic (Pérez et al., 2021; Smith et al., 2010). The northern limb of the ACC (~52 Sv)

follows the SAF through the "54-54 Passage" between Burdwood Bank and Davis Bank (location indicated by the yellow star in Fig. 3A and Fig. 4) to enter the east-west oriented Falkland Through (Nicholson & Stow, 2019; Smith et al., 2010). The SAF-associated current, also referred to as the Falkland Current, is strongly constricted by the bathymetry of the Falkland Plateau, forcing the current across the Plateau with the core paralleling the 1600 m isobath in a general southwest to northeast direction (Nicholson & Stow, 2019). This northward-flowing SAF-Current acts as a major equatorward upper limb of the Atlantic Meridional Overturning Circulation (AMOC) as it transports the relative fresh subantarctic water masses, with AAIW reaching 20°N in the present-day ocean (Fig. 3B; (Chapman et al., 2020; Fischer et al., 2018; McClymont et al., 2016; Voigt et al., 2016). It thereby modifies the heat and salinity budget of the South Atlantic. The Falkland Current also exerts its influence on the Patagonian continental shelf by an onshore intrusion, which leads to a strong thermohaline front between the colder, high salinity water and the warm, relatively fresh shelf water (Piola et al., 2010).

The Polar Front also crosses the North Scotia Ridge into the South Atlantic more to the east through the Shag Rock Passage, transporting 48 Sv, but without making an equivalent equatorward excursion as observed in the SAF (Smith et al., 2010). **C**).

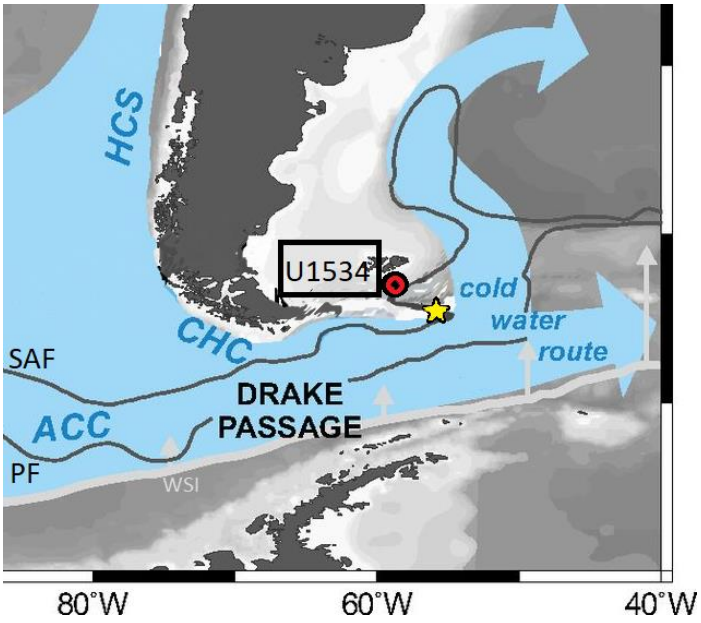

Figure 5. Cold water route as opposed to the position of the fronts. Sea ice obstruction is indicated by grey lines and arrows; enhanced bifurcation of the ACC into the Humboldt Current System during glacial phases; Yellow star indicates the 54-54 Passage between Burdwood Bank and Davis Bank where SAF enters the Falkland Current; Red points are sites from Lamy et al. (2015); Red point with black dot is Site U1534 (figure modified from Lamy et al., 2015

2. Materials

2.1 IODP Expedition 382 Site U1534 locality and setting

International Ocean Discovery Program (IODP) Expedition 382 Site U1534 (53°11.38'S, 58°45.65'W; Weber & Raymo, 2018; Weber et al., 2019; Perez et al., 2021)) is located in the South-west Atlantic, around ~660 km east of the Strait of Magellan, Chile (Fig. 6; Weber et al., 2019). It is situated on the slope of the Falkland Plateau (South Falkland Slope) at the edge of the Patagonian continental shelf, where it forms the northern flank of the east-west trending Falkland Trough. Site U1534 is situated at 605 m water depth, at Common Depth Point (CDP) 10005 on Seismic Reflector Profile SGFI93 (Fig. 8). The sediment recovered at Site U1534 was an almost continuous ~300 m sedimentary section from the crest of the contourite drift. Core U1534 penetrated the thickest part of the crest (Fig. 8 and 9), thus targets the highest sediment accumulation rates to optimize the temporal resolution (Peck et al., 2021; Pérez et al., 2021). Site U1534 is ideally situated to monitor track migrations and intensity of the SAF and to identify the variability of the export of Antarctic Intermediate Water beneath the SAF (via the cold-water route) on a millennial to orbital scale (Weber et al., 2019).

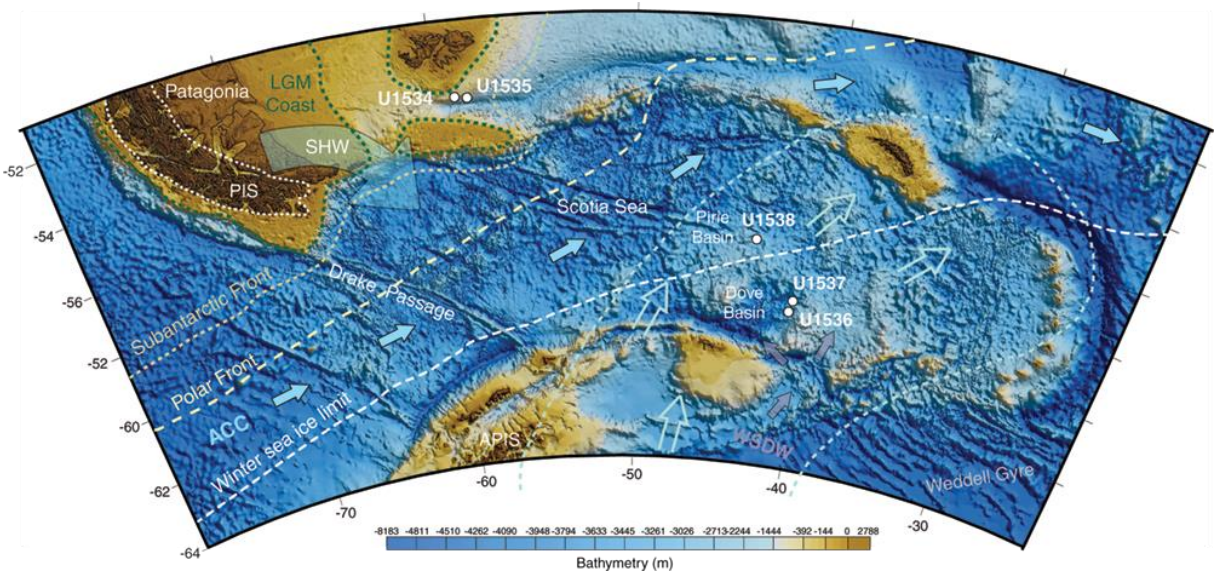

Figure 6. Map of the Scotia Arc with IODP Site U1534 located south of the Falkland Islands in proximity of the Subantarctic Front. Light blue dotted line and open arrows = Iceberg Alley after Anderson and Andrews (1999), large curved grey arrow = main wind direction of Southern Hemisphere westerlies (SHW), light blue solid arrows = Antarctic Circumpolar Current (ACC) flow direction, purple arrows = Weddell Sea Deep Water (WSDW exit route (Maldonado et al., 2003), yellow dotted line = Subantarctic Front, yellow dashed line = Polar Front, green dotted line = Patagonian coastline during LGM (Ilriondo, 2000), white dotted line = limit of Patagonian Ice Sheet (PIS) at LGM (Hein et al., 2010), white dashed line = winter sea ice limit. Satellite bathymetry is shown (Weatherall et al., 2015)" (figure and description from Weber et al., 2019).

2.1.1 Lithostratigraphy

Core U1534 consists of four holes, A, B, C and D, and contains sediments from the Holocene to Pliocene. The shipboard assessment and reports thereafter have described the core lithology of Holes U1534A and U1534C as dominated by greenish-grey silty clays interbedded with clayey silts and clay layers (Fig. 7; Weber et al., 2019; Peck et al., 2021). This study covers the interval from Site U1534 Hole A Core 5H Section 3, 137 cm (mid-depth of recovered core) till U1534A-7H-3, 47 cm; encompassing 36.36 meters below sea floor (mbsf) to 54.46 mbsf; associated with mid-Pleistocene age, broadly covering MIS 12 and 11. Three litho-stratigraphic units were identified (Peck et al., 2021). The first part of the studied interval (0 – 41.74 mbsf) belongs to the litho-stratigraphic Unit I, whilst the second part (41.75 – 54.46 mbsf) falls within Unit II. Lithostratigraphic Unit I has Holocene – mid-Pleistocene age and contains three distinctive carbonate-bearing to carbonate-rich intervals. The third layer is 5 m thick, pale green to light grey biosiliceous ooze abundant in nannofossils and foraminifers and is preliminarily identified as MIS 11 (concurred by the benthic $\delta^{18}O$ data, see Section 2.2.3 Age Model), occurring in Hole U1534A Core 832-U1534A-5H and -6H between 37 and 42 mbsf (also present in Hole C). Biosiliceous silty clays are over- and underlaying the biosiliceous ooze, marked by gradual and partially bioturbated transitions. The base of Lithostratigraphic Unit I is defined by the base of this interval (Peck et al., 2021).

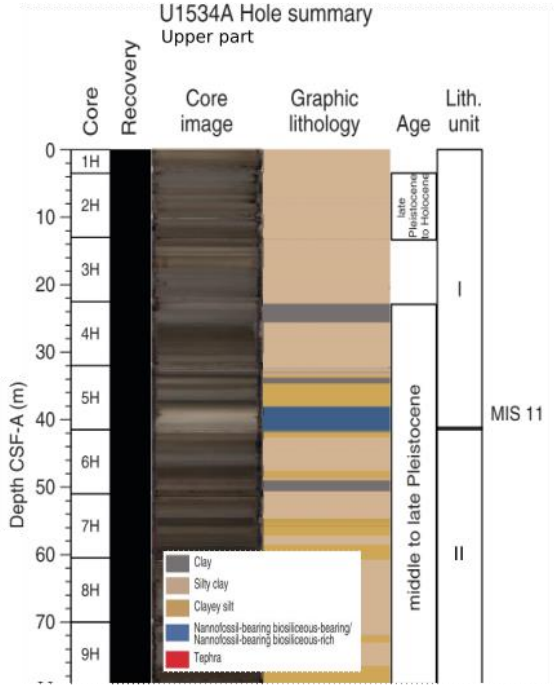

Figure 7. Visual core description, Hole U1534A. CSF-A = core depth below seafloor, Method A (Figure modified from Peck et al., 2021).

The second part of the study interval (41.75 – 54.46 mbsf) is part of Lithostratigraphic Unit II. It has Middle Pleistocene to Late Pliocene, though the study interval only covers a part of the Middle Pleistocene. Unit II starts under the bioturbated transition zone and consists of

biosilica-bearing to biosilica-rich silty clays. The unit contains numerous sharp boundaries between clay-rich and siltier layers. Graded bedding was not found (Peck et al., 2021).

The stratigraphical correlation between the Holes has constructed a new splice to combine data from the different holes. The latest version of the splice (Method-D) is used in this study to obtain the core composite depth below seafloor (CCSF-D) and is used applied in the age model (see Section 2.2 Age model). For a description compilation of splice and CCSF-D depth, see the Methods section on the report of Expedition 382 (Weber et al., 2021). The splice CCSF-depths of U1534 are also available on LIMS Online Report Portal (tamu.edu).

2.1.2 Depositional setting

The Falkland Current is associated with the deposition of extensive contourite drifts on the Falkland Plateau, referred to as the South Falkland Slope Drift (Fig. 8). The contourite drift is deposited beneath the Subantarctic front between ~400 and 2000 m water depth on the northern flank of the east-northwest trending South Falkland Slope. A large slope-parallel erosional moat can be distinguished around the 1600-1700 m isobath (Nicholson & Stow, 2019). The extensive sediment drift above this moat is referred to as the South Falkland Slope Drift (SFSD), where deposition of the contourite drift takes place from ~400 m to 1500 m, while the

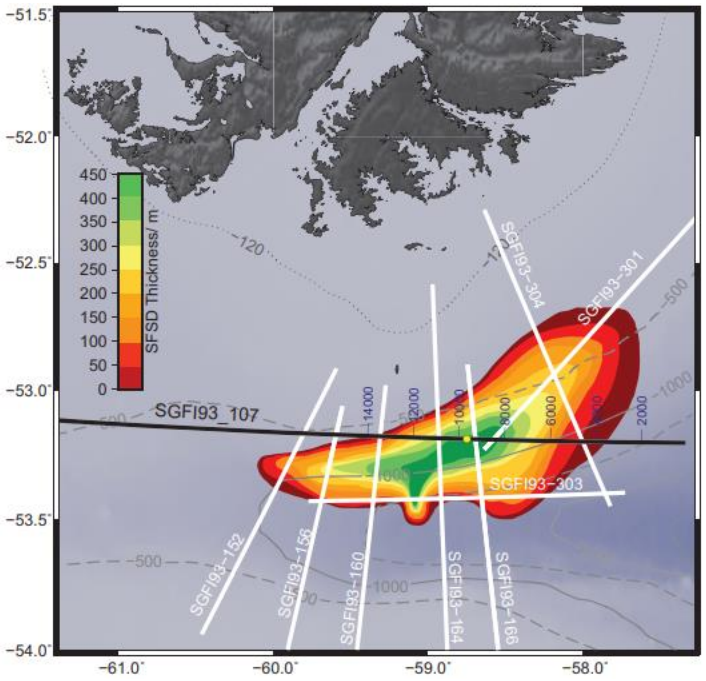

Figure 8. Bathymetry of the South Falkland Slope Drift. The yellow point indicates site U1534. The seismic profile is along Seismic Line SGF193_107 (black line; (Koenitz et al., 2008)) is provided in Fig. 9. (Figure from Weber et al., 2019)

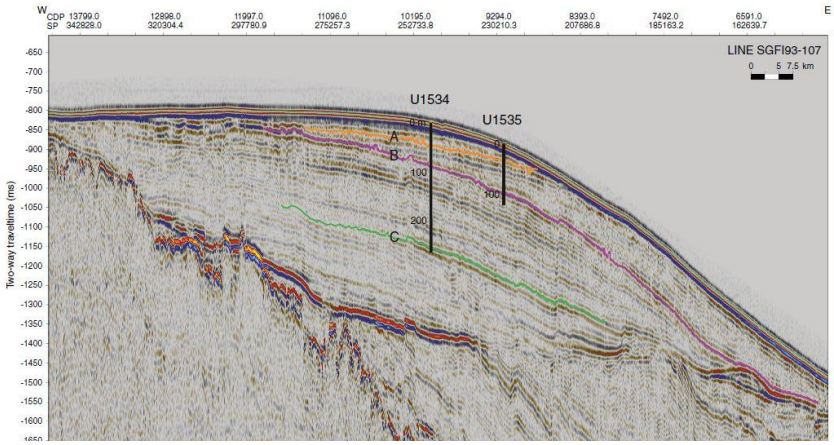

Figure 9. Seismic profile of the South Falkland Slope Drift. The seismic profile is along Seismic Line SGF193_107 (black line in Figure 8. Main discontinuities are marked by Reflectors A (top of Subunit 2A), B (top of Subunit 1B), and C (top of Subunit 1A) (figure Weber et al., 2019).

drift below the moat is referred to as the Lower Falkland Slope Drift (LFSD) (Nicholson & Stow, 2019). Within the seismic profile of the sediment drift are four laterally offset sedimentary units (Fig. 9) evident for an evolving oceanographic setting and bottom current regime (Howe et al., 1997; Pérez et al., 2015).

2.2 Age model

The age model is based on the tuning of benthic foraminiferal $\delta^{18}O$ from U1534 to the global oxygen isotope LR04 stack (Lisiecki & Raymo, 2005); a method routinely applied in modern-day constructions of stratigraphic frameworks of the Quaternary Period (Candy et al., 2014 and references therein). Benthic foraminiferal $\delta^{18}O$ data has been analysed by V. Peck for the Splice of U1534. The splice is described to contain calcareous foraminifers with a rare to relatively persistent occurrence; containing, among other species the infaunal *Uvigerina bifurcata*, *Melonis* spp. and *Hoeglundina elegans* (Peck et al., 2021; Pérez et al., 2021). The interglacials MIS 1, 5, 9 and 11 are particularly represented by the presence of *Melonis* spp. and *H. elegans* with significant low $\delta^{18}O$ values. The glacial maximum of MIS 12 is represented by a $\delta^{18}O$ maximum from *U. bifurcata.*

Biogeochemical tie-points between benthic $\delta^{18}O$ and the LR04 stack are provided by Dr V. Peck for the Holocene and late- to mid-Pleistocene glacial-interglacial cycles, and linear interpolation between the tie-points has resulted in the orbital-scale age model up to MIS 12 (Fig. 10) with the lowermost tie-point set between 49.59 m CCSF-D and 437 ka (Peck, 2021).

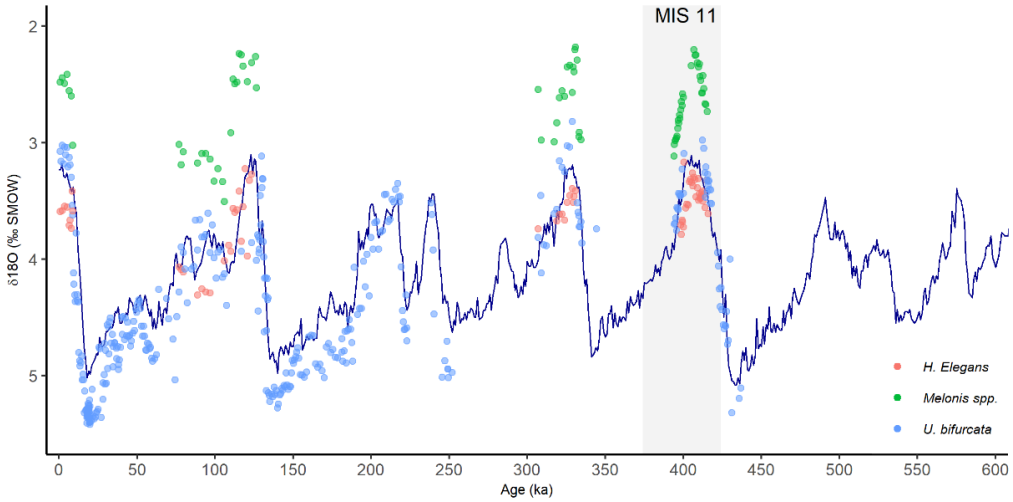

Figure 10. Benthic foraminiferal δ^{18}O data from IODP Site U1534 tuned to the benthic LR04 stack till 437 ka (Lisiecko & Raymo, 2005) by V. Peck (2021). The blue line ls LR04 stack. U1534 δ18O data from three different benthic foraminifera species are indicated by the coloured datapoints. The grey area represents MIS 11

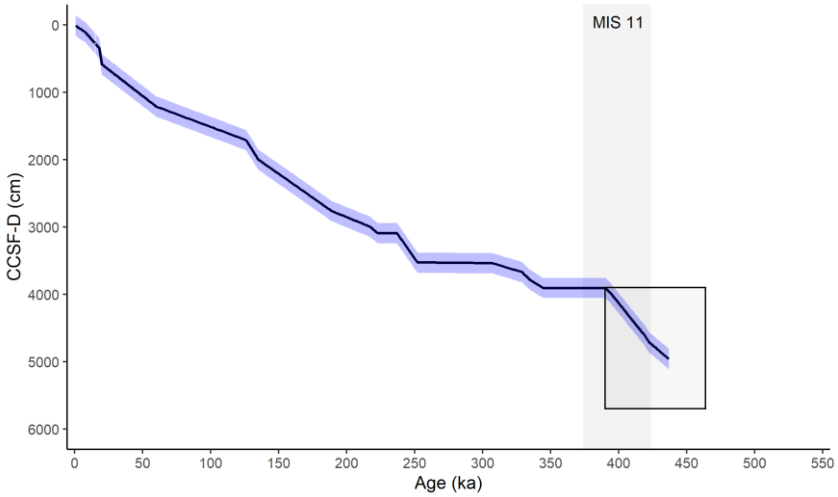

Figure 11. The current age model for U1534 does not cover the entire study interval. grey area represents MIS 11, box represents the study interval. Linear interpolated between tie-points provided by V. Peck.

The current age model does not cover the entire dataset from this study because this study covers the depth interval from 39.04 m to 56.96 m CCSF-D (Fig. 11). To assign ages to samples beyond 49.59 m CCSF-D (>437 ka), I have correlated several additional tie-points between benthic foraminiferal δ^{18}O data from U1534 and the LR04 stack. The main lead for tuning additional tie-points was the strong association of *H. elegans* to warm interglacials, correlating the subsequent minimum of δ^{18}O from *H. elegans* to MIS 13.

The age model reveals three hiatuses. The third spans eliminates the later stage of MIS 11, the entire cold phase MIS 10 and the beginning of MIS 9. I have correlated an additional tie-point

at the side of MIS 11 of this hiatus to improve the resolution because the hiatus sits right on top of the uppermost sample of this study (See Appendix I for the tie-points).

2.3 Samples

This study used 60 sediment samples from IODP Expedition 382 Hole U1534A Core 5H Section 3, 137 cm to Core 7H-3, 47 cm; encompassing 36.36 mbsf to 54.46 mbsf; with converted splice composite depths from 39.04 to 56.96 m CCSF-D. The samples from this section have been analysed for biomarker-based palaeothermometry and palynology. See Appendix I for an overview of the sample from 382-U1534A-5H-3, 137cm to 382-U1534A-7H-3, 47cm.

3. Methods

3.1 Organic geochemistry for GDGT-based palaeothermometry

3.1.1 Sample processing for organic geochemical biomarker analysis

The processing of the samples for organic geochemistry comprised extraction, Al_2O_3 column separation, filtering techniques and analysis, following the procedures of the Geo-lab at Utrecht University, as described in, e.g., (Bijl et al., 2021; Huguet, 2007; Sangiorgi et al., 2018).

In short, sixty freeze-dried sediment slices (~10 g dry weight) were crushed into powder then extracted with dichloromethane : methanol (DCM : MeOH) 9 : 1 (*v*/*v*) in an Ethos X Microwave at a temperature of 70 °C. Al_2O_3 column chromatography separated the total lipid extracts into three fractions using Hexane : DCM 9 : 1 (*v*/*v*), Hexane : DCM 1 : 1 (*v*/*v*), and DCM : MeOH 1 : 1 (*v*/*v*) to obtain the apolar, ketone, and polar fractions, respectively. The fractions were evaporated under an N_2 stream and weighted. The polar fractions were diluted with hexane : isopropanol (99 : 1) and filtered through a polytetrafluorethylene (PTFE) filter. Glycerol dialkyl glycerol tetraethers (GDGTs) and branched GDGTs in the polar fraction were analysed using high performance liquid chromatography mass spectrometry (HPLC-MS) identified by their specific mass-to-charge ratio (m/z). The relative abundances of GTGTs are determined by the integration of peak areas of each individual compound in the mass chromatogram (see Fig. 13 for an exemplary HPLC-MS chromatogram).

3.1.2 TEX_{86} palaeothermometry

TEX_{86} (TetraEther indeX of 86 carbon atoms) is a lipid biomarker-based proxy for sea surface temperature (SST) reconstruction (Schouten et al., 2002, 2013). The TEX_{86} ratio is based on the distribution of isoprenoidal GDGT membrane lipids, biosynthesised by the phylum Thaumarchaeota (Schouten et al., 2013). This prokaryotic group is ubiquitous in the marine realm and most abundant in the thermocline and lower mixed layer (Hurley et al., 2018). Thaumarchaeota biosynthesize isoGDGTs with a varying number of cyclopentyl moieties (Fig. 12). The TEX_{86} ratio has come to development after the verification in core tops that the number of cyclopentane moieties is related to the growth temperature of the micro-organism, shown to be best correlated with annual SST (Schouten et al., 2002). The TEX_{86} ratio is based on the relative abundance of isoprenoid GDGT-1, GDGT-2, GDGT-3 and the crenarchaeol isomer Cren′ (Schouten et al., 2002):

$$TEX_{86} = \frac{\mathrm{GDGT{-}2} + \mathrm{GDGT{-}3} + \mathrm{Cren'}}{\mathrm{GDGT{-}1} + \mathrm{GDGT{-}2} + \mathrm{GDGT{-}3} + \mathrm{Cren'}} \qquad \text{(Schouten et al., 2002) } (1)$$

In the recent year, TEX_{86} has been re-evaluated several times, leading to new proposed calibrations to convert TEX_{86} index values to mean annual sea surface temperatures (0-20 m).

$$SST_{exp}\,(TEX_{86}) = 68.4 * \mathrm{Log}_{10}(TEX_{86}) + 38.6 \qquad \text{(Kim et al., 2010)} \quad (2)$$

$$SST_{lin}\,(TEX_{86}) = 58.8 * (TEX_{86}) - 11.18 \qquad \text{(O'Brien et al., 2017)} \quad (3)$$

The exponential calibration (SST_{exp}; (Kim et al., 2010)) suffers from a dilution bias (Cramwinckel et al., 2018), whereas the linear interpolation (SST_{lin}; (O'Brien et al., 2017)) has solved this, though it is developed for Cretaceous palaeothermometry. This study will therefore focus on the SST_{exp} calibration in the TEX_{86}-SST conversion for its better applicability for the Pleistocene but also incorporate SST_{lin} to indicate the uncertainty of the calibration error and the differences in SST output.

3.1.1 GDGT indices and overprints

Several non-thermal SST sources can affect the isoGDGT distribution in the sediment. Outliers must be eliminated from the record to exclusively assess the isoGDGTs primary produced by near-surface dwelling Thaumarchaeota, discarding non-pelagic contributing sources. The

remainder of the TEX_{86} index results can subsequently be translated into SST values with confidence (Bijl et al., 2021; Cramwinckel et al., 2018; Schouten et al., 2013).

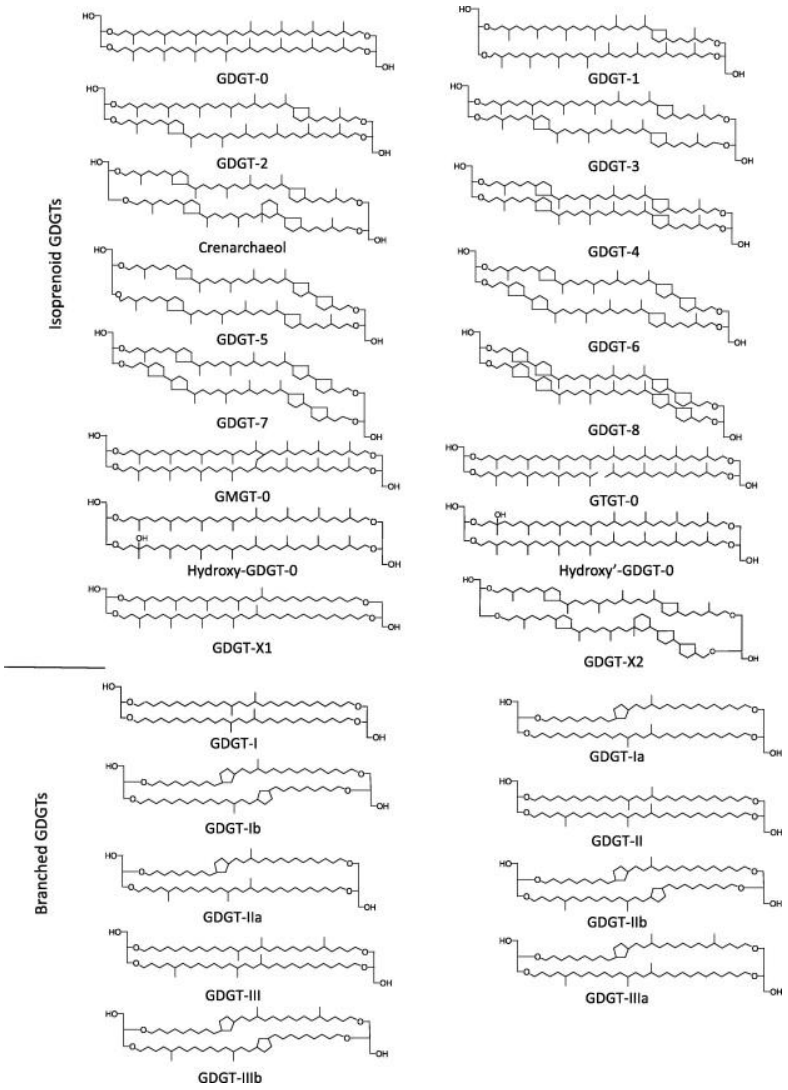

Figure 12. Structure of isoprenoid GDGTs (top), and branched GDGTs (bottom). Figure from Schouten et al. (2013).

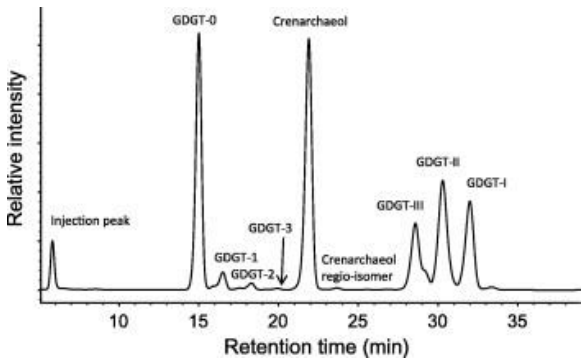

Figure 13. Example of an HPLC-MS base peak chromatogram, indicating the presence and abundance of iso- and brDGDTs (Figure from Schouten et al., 2013).

3.1.2 GDGT indices and overprints

Several non-thermal SST sources can affect the isoGDGT distribution in the sediment. Outliers need to be eliminated from the record to exclusively assess the isoGDGTs primary produced by near-surface dwelling Thaumarchaeota, discarding non-pelagic contributing sources. The remainder of the TEX_{86} index results can subsequently be translated into SST values with confidence (Bijl et al., 2021; Cramwinckel et al., 2018; Schouten et al., 2013).

The indices developed to identify the most known sources of overprints also provide a range of paleoenvironmental information. The Branched vs Isoprenoid Tetraether (BIT) index indicates soil organic matter input to the ocean (Hopmans et al., 2004; modified by Bijl et al., 2021). Index values > 0.3 indicates high terrestrial/fluvial input and possible overprint of marine-derived GDGT signal.

$$\text{BIT index} = \frac{\text{IIIa}+\text{IIIa}'+\text{IIa}+\text{IIa}'+\text{Ia}}{\text{Cren}+\text{IIIa}+\text{IIIa}'+\text{IIa}+\text{IIa}'+\text{Ia}} \qquad \text{(Hopmans et al., 2004) } \textit{(a)}$$

fcren' identifies non-thermal contributors of crenarchaeol isomer to the isoGDGTs (O'Brien et al., 2017). Cut-off value set on > 0.25 excludes non-thermal crenarchaeol contributors.

$$\text{fcren}' = \frac{\%\ \text{Cren}'}{\%\text{Cren}' + \%\text{Cren}} \qquad \text{(O'Brien et al., 2017)} \quad \textit{(b)}$$

The Methane index is a proxy for detecting methane-metabolizing archaea (Zhang et al., 2011), with its cut-off value is set on 0.3.

$$\text{Methane index} = \frac{\text{GDGT}-1 + \text{GDGT}-2 + \text{GDGT}-3}{\text{GDGT}-1 + \text{GDGT}-2 + \text{GDGT}-3 + \text{Cren} + \text{Cren}'} \qquad \text{(Zhang et al., 2011)} \quad \textit{(c)}$$

AOM ratio is used to determine potential influence of anaerobic oxidation methane (AOM) (H Weijers et al., 2011). Values below the cut-off value of 0.2 are considered without overprint from anaerobic methane oxidizers.

$$\text{AOM index} = \frac{\text{GDGT}-2}{\text{Cren}} \qquad \text{(Weijers et al., 2011)} \quad \textit{(d)}$$

Methanogenic overprint is an index for identifying the biosynthesis of GDGT-0 by methanogenic archaea (Blaga et al., 2009). Index values higher than 2.0 could skew TEX_{86} values.

$$\text{Methanogenesis} = \frac{\text{GDGT}-0}{\text{Cren}} \qquad \text{(Blaga et al., 2009)} \quad \textit{(e)}$$

GDGT-2/3 ratio indicates potential water column overprint (Taylor et al., 2013). GDGT production by Crenarchaeota may be affected by seasonality and depth habitat changes of the micro-organisms (Huguet, 2007). Values higher than 5 indicate GDGT biosynthesis affected by seasonality and/or depth habitat of the Crenarchaeota. The cut-off value of 5 is considered to be a conservative cut-off value.

$$\text{Water column overprint index} = \frac{\text{GDGT}-2}{\text{GDGT}-3} \qquad \text{(Taylor et al., 2013)} \qquad (f)$$

The Ring Index (RI) is a proxy for non-pelagic GDGT influence (Zhang et al., 2016). A cut-off value is set on ΔRI >0.3 and depends on a calibration of the TEX_{86} value:

$$\text{RI} = 0 \text{ x } \%\text{GDGT}_0 + 1 * \%\text{GDGT\_1} + 2 * \%\text{GDGT\_2} + 3 * \%\text{GDGT\_3} + 4 * \%\text{ Cren} + 4 * \%\text{Cren}'$$

$$\Delta\text{RI} = \text{RI}_{\text{TEX}} - \text{RI} \quad (\text{RI}_{\text{TEX}} = -0.77 * \text{TEX}_{86} + 3.32 * \text{TEX}_{86}^{\ 2} + 1.59) \qquad \text{(Zhang et al., 2016)} \qquad (g)$$

The ΔRI/TEX_{86} correlation is calculated to determine the source of pelagic derived isoGDGT and has a confidentially interval of <0.95.

3.1.3 Branched GDGT-based palaeothermometry

Temperature relationships between branched GDGTs (brGDGTs) and branched glycolerol monoalkyl glycerol tetraethers (brGMGTs) have mostly been revealed for non-marine environments. Recent studies seek to identify hypothetical temperature relationships for the marine realm, although their appearance is generally sparse (Bijl et al., 2021 and references therein; De Jonge et al., 2019). These ratios are therefore also calculated and presented in this thesis to accommodate in identifying such correlations.

Mean annual air temperatures (MAAT) (De Jonge et al., 2019) are reconstructed for the hinterland using a soil-based MBT'5me-based calibration (Dearing Crampton-Flood et al., 2020).

$$\text{MBT'5me} = \frac{\text{IIIa+IIIb+IIIc}}{\text{IIIa+IIIb+IIIc+IIa+IIb+IIc+Ia}} \qquad \text{(De Jonge et al., 2014a)} \qquad (k)$$

In peats, the relative abundance of brGMGTs to the relative total brGDGTs appears to relate to higher temperatures (Naafs et al., 2018a).

$$\%\text{brGMGT}, \%\text{brGMGT}_{\text{acyclic}} = \frac{[\text{brGMGT}]}{[\text{brGMGT}] + [\text{brGDGT}]} * 100 \qquad \text{(Naafs et al., 2018a)} \qquad (h)$$

Naafs et al. (2018a) also reported for peats a relationship between methylation of brGMGTs and temperature:

$$\text{HMBT}_{\text{acyclic,all}} = \frac{\text{H1020a+H1020b+H1020c}}{H1020a+H1020b+H1020c+H1034a+H1034b+H1034c+H1048} \quad \text{(Naafs et al., 2018a)} \quad (i)$$

And lastly, a strong temperature correlation in tropical lakes is found by Baxter et al. (2018a):

$$\text{BrGMGTI} = \frac{\text{H1020c+H1034a+H1034c}}{\text{H1020b+H1020c+H1034a+H1034b+H1034c+H1048}} \quad \text{(Baxter et al., 2019)} \quad (j)$$

An additional set of indices tests the reliability of brGDGT-based palaeothermometry. The isomerization ratio (IR; De Jonge et al., 2014b) identifies riverine and coastal in situ brGDGT production, for which the cut-off value depends on regional soil values (De Jonge et al., 2014; Sinninghe Damsté, 2016). The $\#rings_{tetra}$ and $\#rings_{penta}$ index (and related indices; Sinninghe Damsté, 2016) use the number of rings, where high values indicate marine in-situ brGDGT production. The cutoff value is set to >0.7.

All indices and calculations are from the methods from Bijl et al. (2021) and acquired using the R markdown from (https://github.com/bijlpeter83/RGDGT .git, last access: 10 November 2021; Bijl et al., 2021), which loads a Microsoft Excel spreadsheet containing peak areas of GDGTs.

3.2 Marine palynology

3.3.1 Palynological sample preparation and analysis

Palynological sample preparation followed the standard techniques of the Laboratory of Palaeobotany and Palynology at Utrecht University. For a total of 59 freeze-dried, powdered samples (~ 10 g dry weight sediment), a *Lycopodium clavatum* tablet with a known number of spores (n = 19855 ± 4.1% spores per tablet) was added for quantification of dinocyst abundances (Wood et al., 1996; Sangiorgi et al., 2018). The samples were treated with 30% HCl (hydrochloric acid) and unheated 38% HF (hydrofluoric acid) to dissolve and remove carbonate and silica. The organic residues were sieved over a 10 µm nylon mesh during treatment in an ultrasonic bathtub. An aliquot of the sieved organic residue was transferred by pipette onto a microscopic slide using glycerine jelly as a mounting medium.

59 microscopic slides have been analysed under an optical light microscope at 400x magnification. Preferably 200-300 dinocysts are counted per slide, though a substantial portion

of the samples had relatively low dinocyst yield, and for these slides, only 50-100 dinocyst specimens were counted. Due to time limits, only a part of these relatively barren slides has ultimately been analysed, which is still found relevant because if not studied, the downcore dinocyst distribution would only reach 430 ka, and the glacial maximum of MIS 12 (and older) would be discarded. Nevertheless, careful interpretation of these barren samples should be taken into account because of the low dinocyst yield; however, they are still retained in the dataset.

The absolute abundance of in situ dinocysts is determined by calculating the concentration (dinocysts per gram dry weight) following the equation of (Benninghof, 1962) using the amount of *Lycopodium clavatum* spores counted in the slide and the number of *Lycopodium clavatum* spores present in the batch (n = 19855):

$$In\ situ\ dinocyst\ concentration\ = \frac{\text{total in situ specimens}}{n.\ Lycopodium\ clavatum\ \text{spores}} * \frac{19855}{weight(g)}\ (\text{cysts*g}^{-1})$$

In situ dinocyst counts were transferred into percentages based on the total in situ dinocysts to detect relative abundances within the assemblage and to allow comparison with reference datasets of modern assemblages (Esper & Zonneveld, 2007; Prebble et al., 2013; Thöle et al., 2022 (in prep)).

A large number of samples contained a remarkably high amount of reworked specimens, comprising Eocene to Pliocene (Paleogene – Neogene) taxa (such as *Deflandrea* spp.). Therefore, the reworked dinocyst concentration (reworked cysts per gram dry weight) is also calculated. The percentages of in situ versus reworked dinocysts are determined based on the sum comprising both in situ and reworked dinocysts to identify the potential impact of reworked material on the interpretation of the in situ specimens.

Taxonomy, nomenclature and grouping

Dinoflagellate cyst taxonomy and nomenclature followed (Marret et al., 2019; Marret & Zonneveld, 2003; and references therein); the PALSYS database (available at https://palsys.org/genus) and the online Marum Zonneveld Atlas (Zonneveld, KAF and Pospelova V., 2015, available at https://www.marum.de/en/Karin-Zonneveld/Modern-Dinocyst-Key.html). Identification is determined to species level where possible, while taxa grouping is based on morphological and ecological affinity following previous work from

Marret and Zonneveld (2003), Prebble et al. (2013), Zonneveld et al. (2013), Zonneveld and Pospelova., 2015; Marret et al. (2019); and Thole et al. (in prep). See Table 1 for an overview of identified dinocysts, groups, and their biogeographical affinity (biogeographical affinity is further elaborated in the next section 3.3.2).

The following dinocyst taxa were grouped:

- *S. mirabilis* and *S. mirabilis* CF (or *S. hypercanthus?*), the latter being probably *S. mirabilis* but without the characteristic 'crown' being recognized or present due to bad preservation or folding, as argued by K. Zonneveld (Esper & Zonneveld, 2007). *Achomosphaera* was also considered to be grouped together with *S. mirabilis*, as first it was thought that these were not recognized as *S. mirabilis* due to similar reasons. However, this species may just as well be a non-Pleistocene *Spiniferites* spp. Nevertheless, *S. mirabilis*, *S. mirabilis CF* and *Achomosphaera* generally do follow the same trend and reach similar, relatively high percentages.
- *Spiniferites* complex (cpx.) comprise all *Spiniferites* and *Achomosphaera* spp. for comparison with other assemblages and clusters.
- All *Impagidinium* spp. are grouped together, except *I. pallidum*.
- *I. pallidum* is grouped together with *D. chathamensis*.
- *O. centrocarpum* comprises all *Operculodinium* spp.
- *N. labyrinthus* comprises all *Nematosphaeropsis* spp.
- *S. quanta* is taken together with the more transparent *S. quanta* version. I first identified them separately, but the difference is probably due to oxygenation/degradation processes; however, very brown specimens could potentially be reworked. Initially they were counted separately, but are here taken together for comparison with other assemblages.
- *Islandinium minutum*, *Islandinium spp.* and *Echnidinium* spp. Unsure classification also led to the assigning of specimens to *Islandinium* spp. but are most likely *I. minutum*. Confusion of identification may have led to misclassifying *Islandinium minutum* as *Echnidinium* spp., and are therefore grouped together.

3.3.2 Environmental interpretation of the dinocyst assemblage distribution

Oceanic productivity trends are strongly indicated by the distribution of two main types of dinocysts in Southern Ocean surface sediments (Esper & Zonneveld, 2007; Harland & Pudsey, 1999). Protoperidinioid (P) dinocysts are (likely) produced by heterotrophic dinoflagellates and predominantly include the genera *Brigantedinium* and *Selenopemphix*. P dinocysts reach peak abundance in the SAZ and AZ during or immediately after peaks of autotrophic biomass concentrations. They are primarily restricted by the STF as their northern limit (Marret & Zonneveld, 2003; Prebble et al., 2013). Gonyaulacoid (G) dinocyst are commonly produced by phototrophic dinoflagellates mainly represented by *Spiniferites* spp., *Nematosphaeropsis labyrinthus*, *Impagidinium* spp. and *Operculodinium* spp. (Marret & Zonneveld, 2003; Sangiorgi et al., 2018). The phototrophic G dinocysts generally occur in the STZ and SAZ, largely restricted by the PF as their southern limit.

The compilation of ecological/biogeographical affinities of modern species and assemblages is achieved by statistically linking the modern biogeographic occurrence of dinocyst in surface sediments to modern oceanographic conditions (Esper & Zonneveld, 2007). This has led to a globally covering dataset (Marret & Zonneveld, 2003; Marret et al., 2019), and a dataset focussing on the Southern Hemisphere (Prebble et al., 2013; Marret et al., 2019; Thöle et al., in prep). Recent input by Thöle et al. (in prep) has extended the most recent Southern Hemisphere dataset (sh_655; Thöle et al. (in prep), and provides a 9-cluster solution for biogeographic affinities based on k-mean analysis. An additional sub-dataset ("wsi_100"; Thöle et al. (in prep) focusses on ice-proximal sites south of 60°S, and contains a 5-cluster solution. The modern dinocyst clusters relate to key zones with tight oceanographic parameters, generally describing transitions in surface oceanographic conditions from pole to equator, with a quasi-latitudinal orientation. An overview of the modern "sh_655" 9-clusters and "wsi_100" 5-clusters (Thöle et al., in prep) is provided in Appendix III.

The palaeoenvironment interpretation of the palaeo-assemblage distribution of U1534 is mostly based on the comparison with the modern clusters from "sh_655" and "wsi_100". The 5-cluster solution for wsi_100 may seem less applicable on Site U1534 since its latitudinal position at ~53°S, but it could detect glacial extend during MIS 12. Accordingly, when interpreting palae-oceanographic conditions of the dinocyst assemblages, it should be

considered in its full context, including the impact of particle transport and SST (Thöle et al., in prep).

Table 1. Dinocysts groups from U1534 and their biogeographic interpretation.

Group	Dinocysts	Biogeographical affinity
Spiniferites **cpx**.	*S. ramosus* *S. mirabilis (& S. hyper-canthus?)* *Achomosphaera?* *S. bentorii* *S. elongatus*	Cosmopolitan; greatest abundance within or north of the STF; shore-proximal settings; dominate warm waters of ~29°C
Impagidinium **spp.**	All *Impagidimium spp.* except *I. pallidum*	Open marine; generally lower latitudes; highest abundance beneath/near STF; dominate in water of ~22°C
O. centrocarpum	All *Operculodinium* spp.	Cosmopolitan open ocean; no clear geographical boundaries; abundant in waters with SST of ~18-22°C
N. labyrinthus	All *Nematosphaeropsis* spp.	Generally present between 40 and 60°S; well-ventilated bottom waters in Southern Ocean; hotspot along the South American West coast; characteristic for water around 11-12°C
S. quanta	*S. quanta,* *S. quanta* transparent version	High nutrient availability; eutrophic regions, including upwelling areas as well discharge plumes; ventilated bottom waters
I. pallidum cpx.	*I. pallidum* *D. chathamensis*	Max. relative abundance near polar fronts; indicator of reduced salinity due to vicinity of melting sea ice (north of maximal sea ice extension); high [P] and [N], but low chlorophyll-a; well ventilated bottom waters.
Islandinium cpx.	All *Islandinium* and *Echnidinium* spp.	Indicator for sea ice and iceberg transport; dominance is restricted to "Iceberg Alley"; SST <0°C
S. nephroides		Highest abundance beneath STF; High nutrient availability
S. antarctica		Antarctic Zone; indicator for sea ice presence; SST < 0°C, up to 10°C in summer, but dominant in water with SST < -2°C

***Brigantedinium* spp.**	All *Brigantedinium* spp.	Cosmopolitan; high nutrient availability; can dominate from coastal regions to the central parts of the oceans, no clear environmental boundaries; also present at high latitudes; most abundant in waters of 10-15°C
Remaining dinocysts:		
Other (pre-cingular) gonyaulacoid cysts	*Bitectatodinium tepikiense* *Filispaera filifera* *Habibacysta tectata* *Pentapharsodinium dalei* *Pyxidinopsis psilata* *Pyxidinopsis reticulata* *P. palstilliformis*	Outer shelf offshore

4. Results

4.1 Age model

Additional tie-points have been correlated between benthic foraminiferal $\delta^{18}O$ from the Splice U1534 to the benthic LR04 stack (Fig. 15) to assign ages to samples beyond 49.59 m CCSF-D and to increase the resolution around the hiatus of MIS 10. The updated age model for Site U1534 (Fig. 16) spans from 0 to 5700 m CCSF-D, with corresponding ages of 0 to 490 ka. The 60 samples from this study are estimated from 390 to 467 ka with an average temporal resolution is ~1,300 years.

The sedimentation rate at Site U1534 is calculated based on the age model between 10 and 15 cm/kyr during the mid-late Pleistocene, which is in accordance with the estimated sedimentation rates (Peck et a., 2021; in the order of 10cm/kyr) for the South Falkland Slope Drift during this period. In contrast, late Pliocene sedimentation rates were estimated at least 35-40 cm/kyr (Weber et al., 2019; Peck et al., 2021). The effect of sediment compaction is clearly visible in the upper ~120 meters, but reduces at greater depth.

The age model has revealed three hiatuses, which removed sediments mostly during glacial phases. The topmost hiatus is small and spans only 10 kyr around 225 ka; the second spans from ca. 250 to 305 ka, associated with MIS 8; and the third from ca. 345 to 390 ka. The latter is

most relevant for this study, as sits right on top of the uppermost sample of this study (39.05 m; 390 ka). This hiatus eliminates the later stage of MIS 11, the entire cold phase MIS 10 and the beginning of MIS 9.

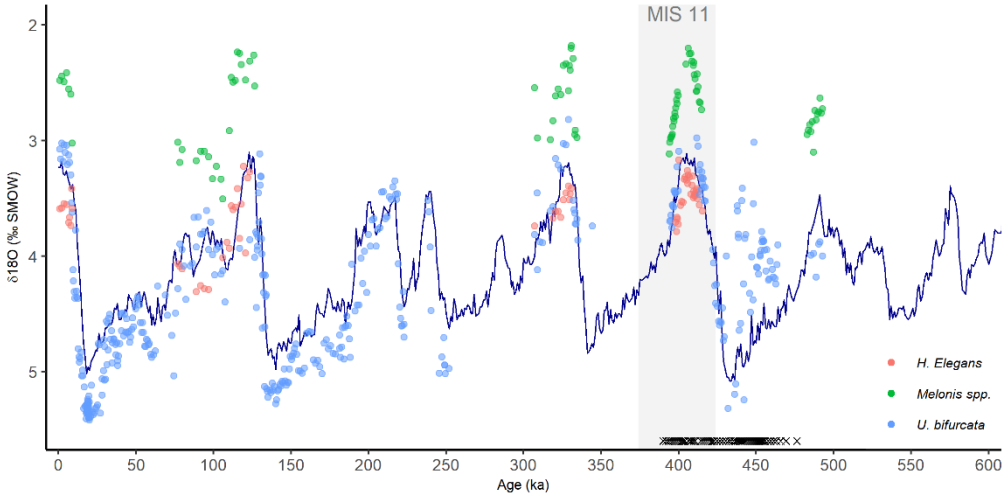

Figure 14. **Updated correlation of benthic foraminiferal δ18O from IODP Site U1534 to the benthic LR04 stack** (Lisiecki & Raymo, 2005), reaching to 490 ka (previously till 437 ka); the grey area represents MIS 11; the black crosses on the x-axis represents the samples from this study.

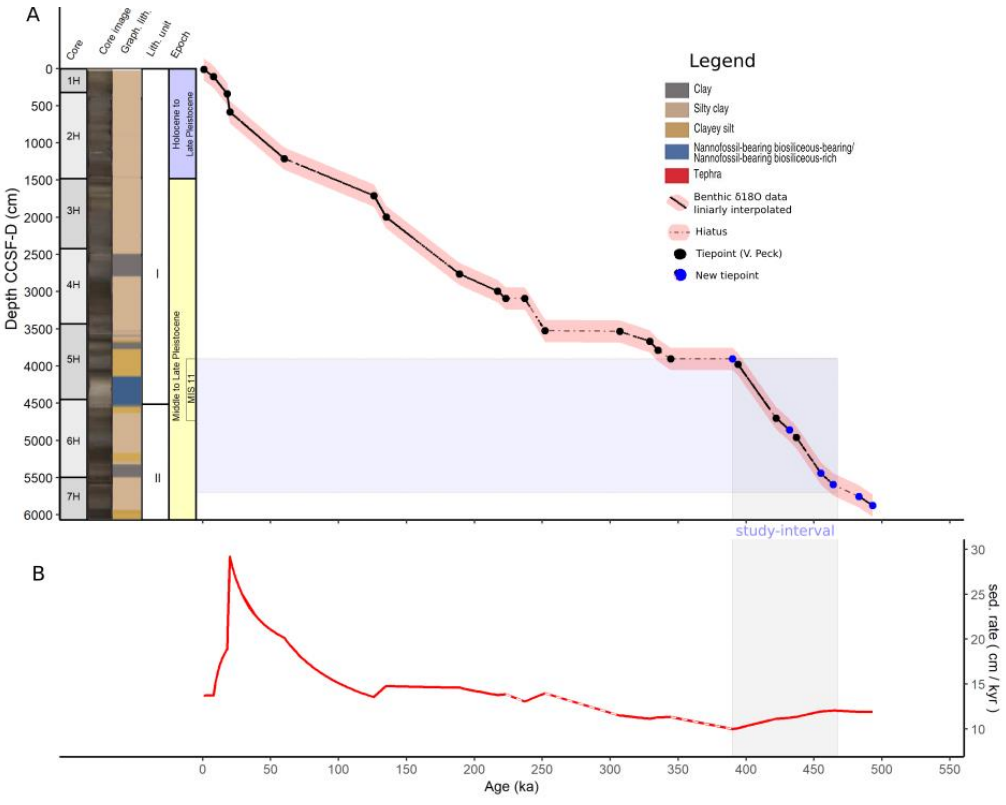

Figure 15. Age-depth model (A) and sedimentation rate (B) for Site U1534. The black line consists of benthic $\delta^{18}O$ datapoints from Site U1534 linearly interpolated to the LR04. The age-depth model interpolates between tie-points as provided by V. Peck (black dots), and an additional set of tie-points (blue dots). The grey area represents the study interval (494-467 ka). Core composite depth below seafloor (CCSF) is in cm. Age in thousand years ago (Ka). Sediment rate in cm per thousand year (cm/kyr). The dashed lines indicate the three hiatuses.

Some insecurity of the age model rests on the presence of hiatuses. Since there were hiatuses during glacial phases, there might very well be a hiatus somewhere during MIS 12. The glacial maximum of MIS 12 is recorded with confidence in Core U1534 as $\delta^{18}O$ (from *U. bifurcata*) exceeds 5‰ SMOW, which correlates well to the benthic LR04 stack, but $\delta^{18}O$ U. bifurcata data from beyond 49.8 m CCSF-D (>437 ka) is correlated with less confidence. The tie-points mainly rest on the correlation between *H. elegans* and MIS 13. However, *H. elegans* has 'skipped' an interglacial before, namely MIS 7, and might just as well have skipped MIS 13 and thus be correlated to MIS 15. This would imply an unidentified hiatus before the glacial MIS 12.

4.2 GDGT-based palaeothermometry

4.3.1 Evaluation of GDGT distributions and indices

Lipids in the polar fraction predominantly consists of isoprenoid GDGTs (Fig. 16). GDGT-0 and Crenarchaeol dominate the GDGT pool, while BrGDGTs and BrGMGTs are < 5 %.

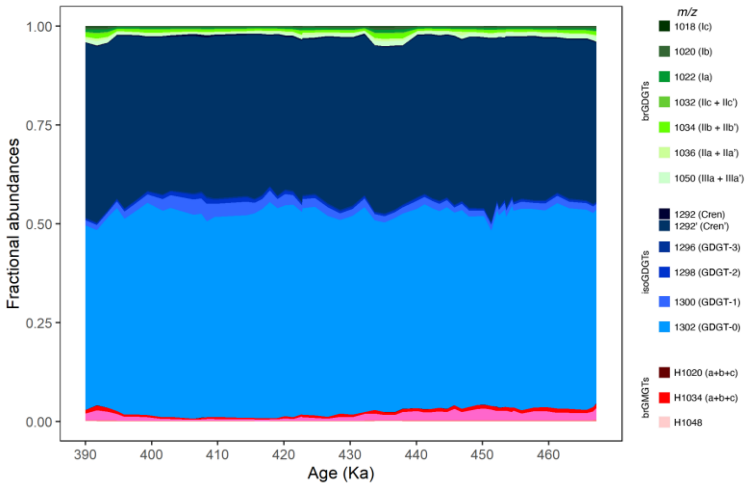

Figure 16. Variations in fractional abundances of the branched (green shades) and isoprenoid (blue shades) GDGTs, and branched GMGTs (red shades) at Site U1534. Figure obtained in the R-markdown from (Bijl et al., 2021).

The analysis of the GDGT distribution by means of the GDGT indices points out that all datapoints fall well below their cut-off values (Fig. 17) and are within the acceptable range of $\Delta RI/TEX_{86}$ (Fig. 18). Accordingly, no potential overprints are detected in the data, hence, a pelagic-derived isoGDGT composition can be confirmed and no samples are discarded for the translation of TEX_{86} values into SST values (Bijl et al., 2021).

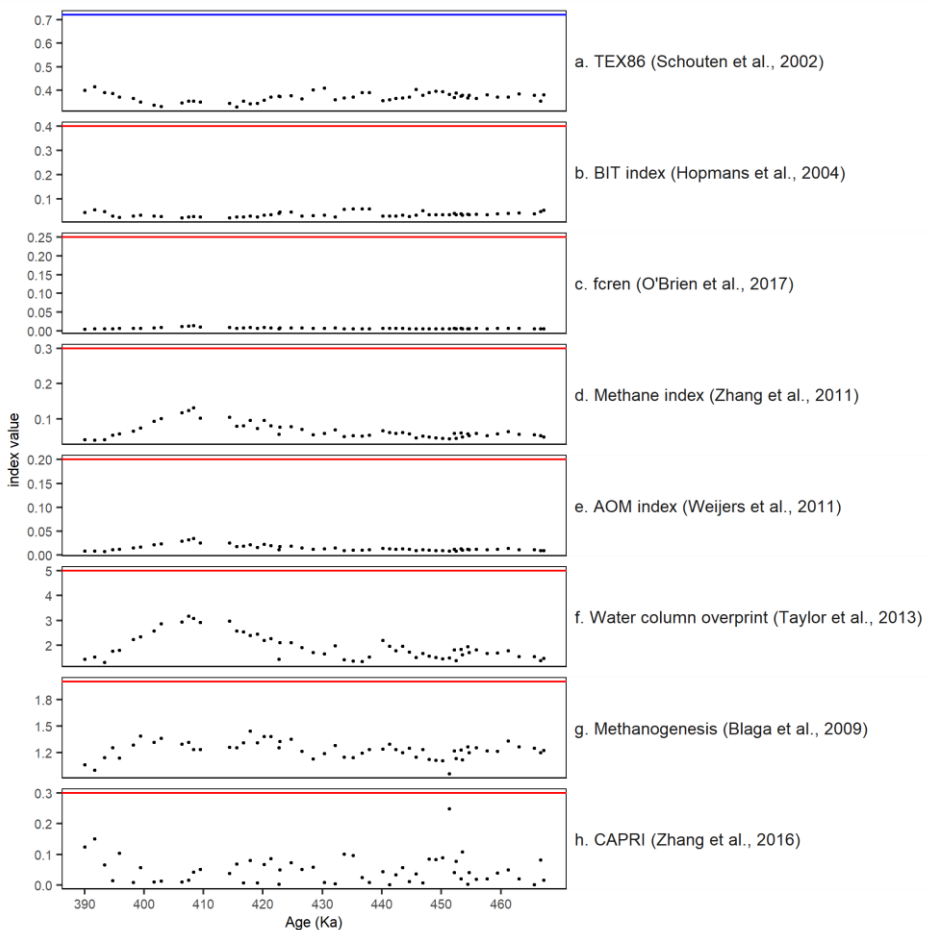

Figure 17. Index values and GDGTs indices to identify overprints. See Methods section 3.1.4 for the equations. Cut-off values per index are indicated by the red lines; no datapoints above the red lines indicate no samples exceeded the cutoff values, thus no samples are discarded. (a) TEX86 (Schouten et al., 2002); maximum modern core-top value (~0.72) is indicated by the blue line. (b) BIT index (Hopmans et al., 2004). (c) fren'(O'Brien et al., 2017). (d) Methane index (Zhang et al., 2011). (e) AOM ratio (Weijers et al., 2011). (f) GDGT-2/3 (Taylor et al., 2013). (g) Methoanogenesis (Blaga et al., 2009). (h) ΔRI (Zhang et al., 2016). Figure obtained by the R-markdown from (Bijl et al., 2021).

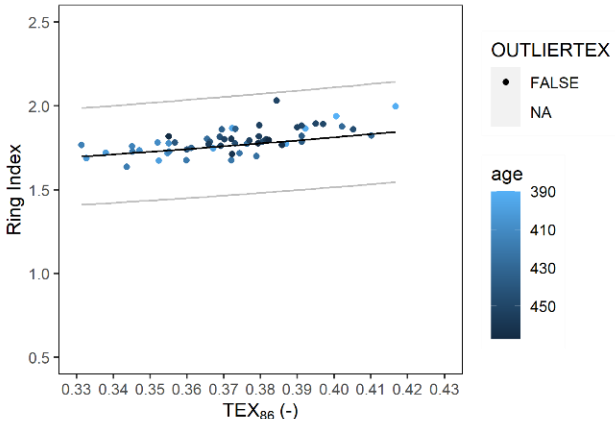

Figure 18. Ring index (RI) vs. TEX86. Dots indicate RI/TEX86 values for all samples, since no samples exceed the indices' cut-off values (see figure 12). Samples are neither discarded by the RI/TEX86 index, indicated by the absence of crosses. Colour of all data points indicate age of the sample, from 390 ka (light blue) to 367 Ka (dark blue). Black and grey curves represent the RI/TEX86 index ratio in modern core-top samples and the 95% confidence interval, respectively. See Methods section 3.1.2 for the index formulas

Nevertheless, some light trends (though under the cut-off values) and co-variances may be detected, namely for the methane index (in lesser degree) and the GDGT-2/3 index. Although it remains below the cut-off value of 5, this trend shows the largest amplitude of all indices, reaching a peak of ~3.2 around 405-410 ka. The water column overprint may therefore be considered when interpreting the data. Lastly, the methanogenic overprint (Fig. 17g) and the Ring Index values (Fig. 17h) are also below cut-off value, and although they show some fluctuation, no clear trend can be detected.

4.3.2 TEX_{86}-based sea surface temperature reconstruction

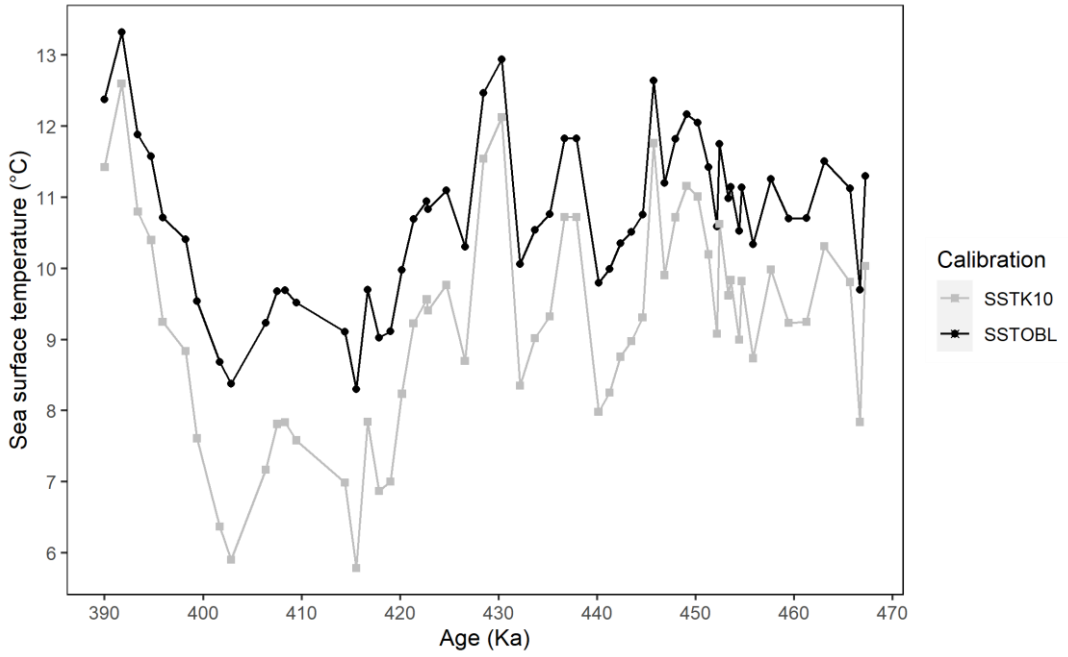

Figure 19. TEX_{86} sea surface temperature (SST) reconstruction of site U1534 using two calibrations; $SST_{lin}(TEX_{86})$ is the black line obtained by the calibration from O'Brien et al. (2017); $SST_{exp}(TEX_{86})$ is the grey line acquired by the calibration from Kim et al. (2010

TEX_{86}-based SST record (Fig. 19) portrays a clear, but counterintuitive trend for a glacial-interglacial cycle. The $SST(TEX_{86})$ pattern is cooling pattern during MIS 11, mirrored to the Antarctic Ice Core temperature reconstruction (EPICA: Wolff et al., 2010), thus opposite to the general warming pattern of MIS 11.

SST estimates obtained by the exponential calibration from Kim et al. (2010) are lower but more fluctuating than the linear calibration from O'Brien et al. (2017). SST_{exp} estimates range between a minimum of 5.8 °C and a maximum of 12.6 °C, while the smaller SST_{lin} depicts a

smaller range, between 8.4 °C and 13.3 °C. The difference between the two calibrations in the colder part of the record about 2°C, and in the warmer part <1°C.

The $SST_{exp}(TEX_{86})$ estimates for MIS 12 are about 8-10 °C. SST_{exp} briefly rises during Termination V to 12 °C at 430 ka, but displays a cooling pattern towards MIS 11 reaching a minimum of ~6°C. SST_{exp} remains relatively low (6-8 °C) during the interglacial MIS 11c. Only at the later stage of MIS 11, from 403 ka onwards, is a SST increase of ~7 °C observed, which appears to be a belayed SST warming in the interglacial.

4.3.3 brGDGT-based palaeothermometry

BrGDGTs en brGMGTs have low relative abundances in the samples of U1534 (<5%; Fig. 16). Indices to discrimination between river in situ brGDGT production (De Jonge et al., 2014b; Sinninghe Damsté, 2016) and marine in situ brGDGT production (Sinninghe Damsté, 2016) have been tested (Fig. 20). The samples have relatively high IR values (De Jonge et al., 2014b; Sinninghe Damsté, 2016), between 0.4 and 0.7 and peak around 400-415 ka. South American soil values are quite fluctuating, between 0.0 and 0.67 in Brasil, 0.25-0.35 for Uruguay, but no soil value from sites nearby the Falklands. For exploratory purposes, the soil value cut-off is set on the highest soil value reported in South America, >0.67. No samples are identified as outlier in this case, but samples from ca. 400 to 420 ka should be taken into consideration for potential riverine brGDGT input.

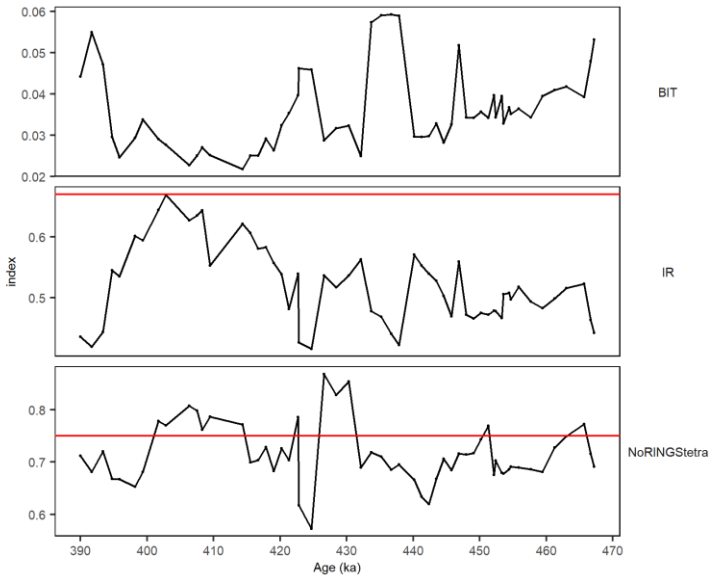

Figure 20. BrGDGT indices and overprints. (upper) BIT index; (middle) IR (with cutoff value of the highest recorded South American soil IR of 0.67, which is very progressive (see text). And red points indicating discarded MAAT samples; #ringstetra with cutoff value >0.75; from Site U1534

Samples have high #rings$_{tetra}$ values and exceed the cut-off value of 0.75 between ca. 402 to 415 ka and around 430 ka, suggesting riverine influx of brGDGT at these time intervals. These samples are thus excluded from the dataset for MAAT. The remaining samples are also high, and close to the highest soil value. Therefore, they could be biased by production in the marine realm. IR$_{hexa}$ and IR$_{penta}$ cross plots of these indices are provided in Appendix IV. It can be concluded that MAAT reconstruction cannot be proceeded with confidence. See Appendix V for the MAAT record with the samples with #rings$_{tetra}$ >0.75 discarded using the MBT'$_{5me}$ calibration from Dearing Crampton-Flood et al. (2020).

For the explanatory purpose of detecting potential temperature trends, brGDGT are presented in Fig. 21. The temperature records obtained by the indices from brGMGTs as proposed by Naafs et al. (2018) and Baxter et al. (2019), result in generally similar trends as the TEX$_{86}$-based SST reconstruction. Although BrGDGTs and brGMGTs are produced in the marine realm in much sparser abundance than isoGDGTs, their pattern suggests hypothetical temperature relationships.

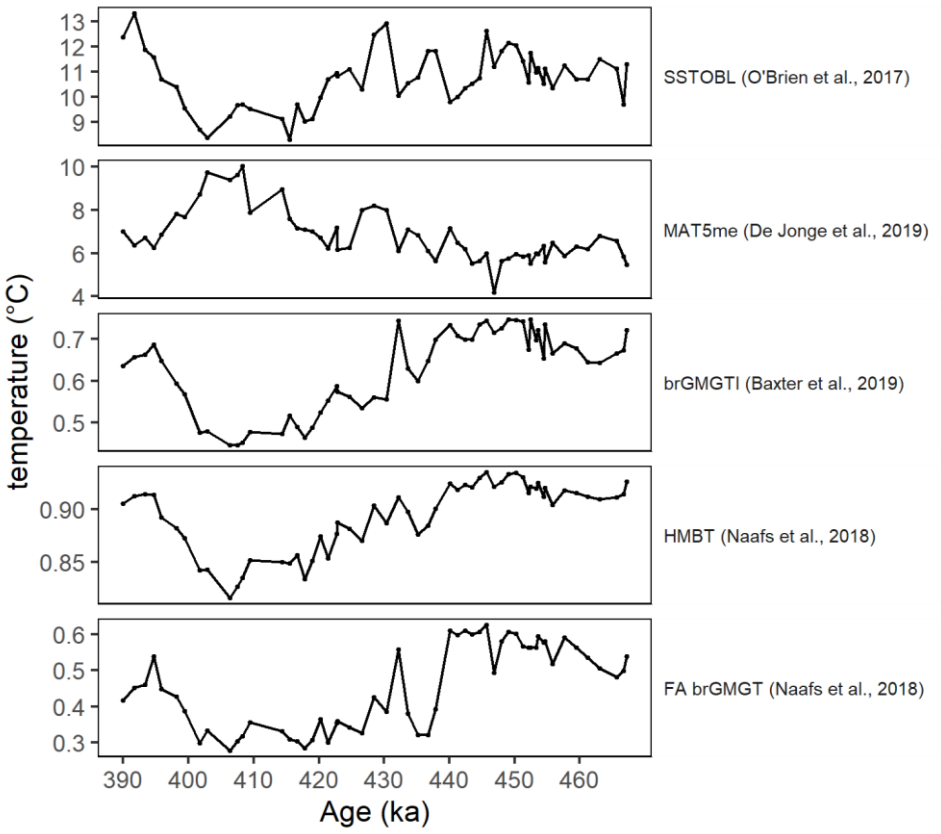

Figure 21. Several brGMGT-based paleotemperature records for U1534.

4.4 Dinocysts assemblage

4.5.1 Palynological sample coverage

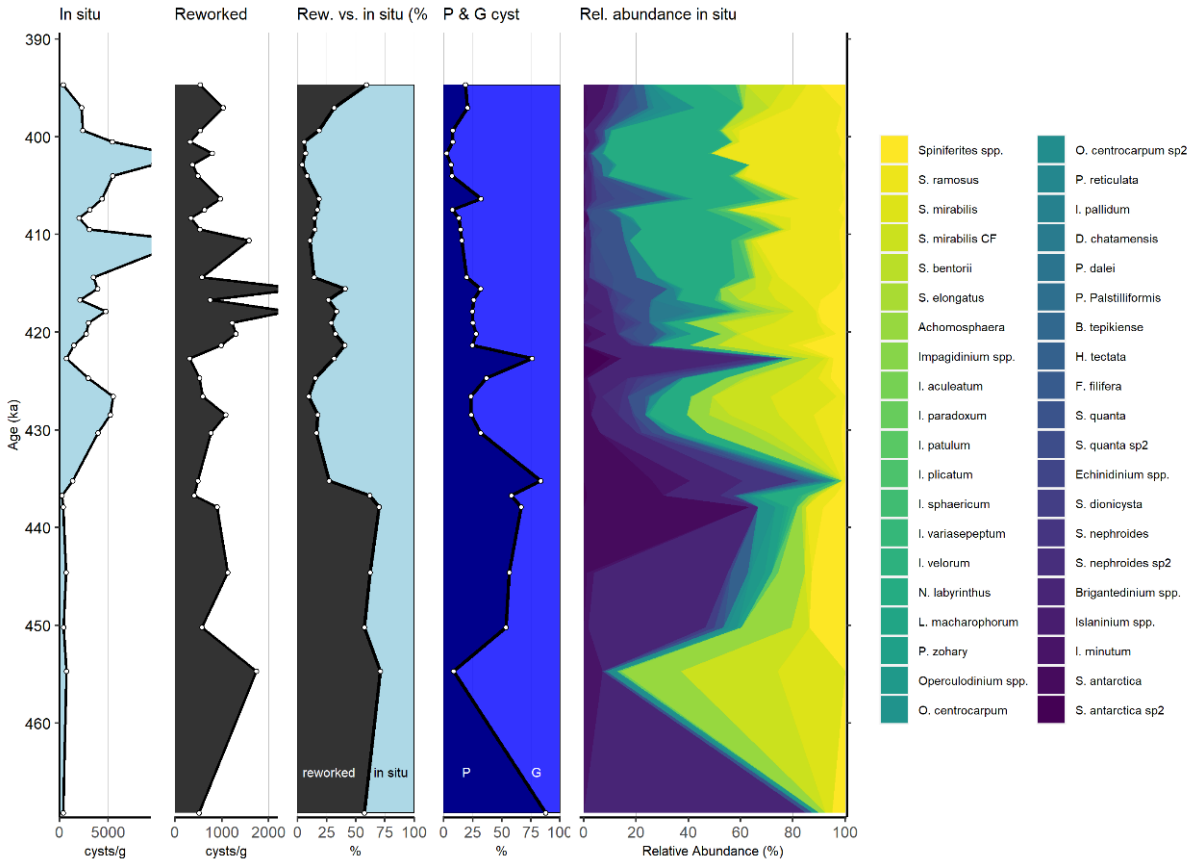

Figure 22. Dinocyst assemblage of U1534A; in situ dinocyst concentration (cyst*g^{-1}); reworked dinocyst concentration (cyst/g); reworked vs. in situ portion (%) of the total dinocysts; P-cysts vs. G-cysts; the relative abundances of total in situ dinocyst assamblage. The white points represent the analysed datapoints (counted samples).

31 of the 59 samples have been examined (see the white datapoints in Fig. 22). The study interval from 437 to 394 ka (49.83 - 39.65 m CCSF-D), has been analysed in high resolution of ~1,000 years. This section covers MIS 11, Termination V, and the glacial maximum of MIS 12. The study interval beyond the glacial maximum (>437 ka; >49.83 m CCSF-D), is analysed in lower temporal resolution of ~ 6,000 years.

Samples from MIS 12 and older (>430 ka; >48.3 m CCSF-D) were relatively barren and had low census count, 50-100 specimens (see Appendix I for census counts). The percentage of reworked material was particularly high, between 60 – 70%. Samples from the upper, high-resolution study section (<430 ka; < 48.3 m CCSF-D) contained generally high in situ dinocyst yield (Fig. 22). Percentage of reworked material in this section is lower, between ~5 and 35%.

4.5.2 In situ dinocyst assemblage

A notable change in the dinocyst assemblage is displayed on glacial-interglacial timescale. The glacial phase of MIS 12 is dominated by *S. antarctica*; Termination V displays an increase in biodiversity and a transition from P- to G-dinocysts dominance; and MIS 11 is mainly represented *N. labyrinthus* and *S. ramosus* (See Appendix V for the total in situ relative abundance distribution). The assemblage is compared to modern clusters from Thöle et al. (in prep), as discussed below (Fig. 23). Spiniferites spp. are abundant throughout all samples, except MIS12 glacial maximum.

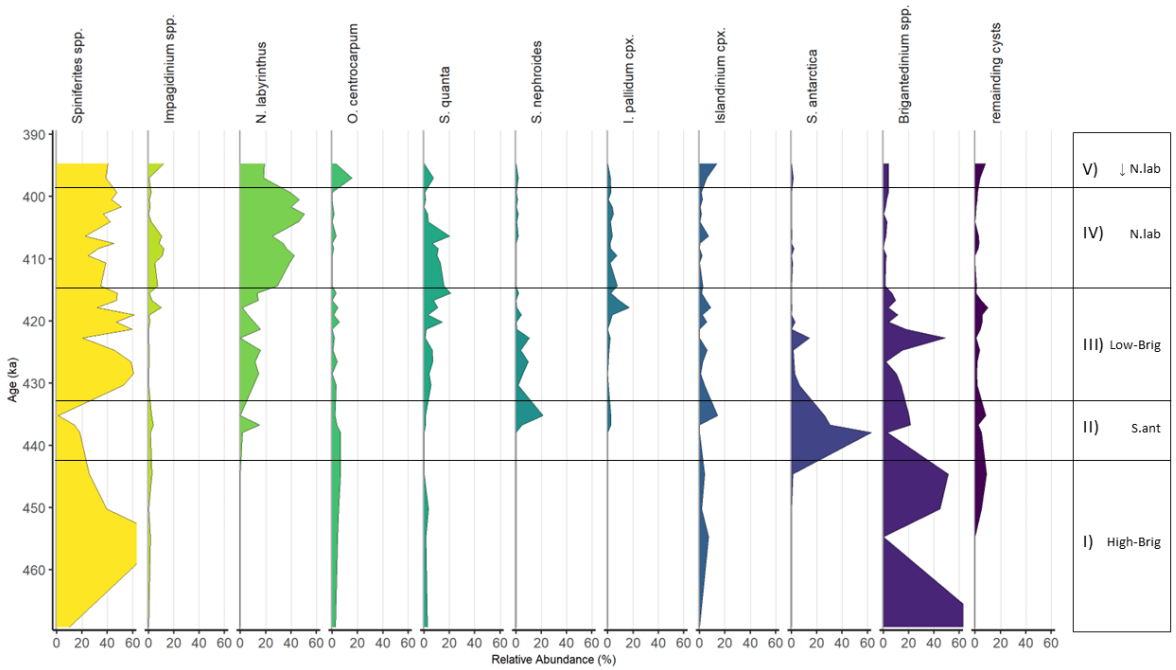

Figure 23. Relative abundances of the main dinocyst taxa from U1534. On the right are the clusters from SH-655 (Thöle et al. (in prep) that the assemblages are assigned based on similarities, and indications of rising or decreasing relative abundance of prominent taxa. I) is assigned High-Brig-Cluster but with an interval of high *S. mirabilis*; II) is Sant-Cluster; III) is low-Brig-Cluster; IV) is Nlab-Cluster; VI) has no clear cluster assigned.

I) Brigantedinium spp. dominate preceding MIS 12

Brigantedinium spp. is the largest representative of P dinocysts, and dominate the barren samples from greater depth than 49.83 m, older than 437 ka. *Brigantedinium* spp. have a relative abundance of ~40 to 80%. Other dinocysts in this sample's assemblage only reach small abundances (<10%), comprising *Spiniferites* spp. *Operculodinium centrocarpum* and *Selenopemphix quanta*. This sample is most similar to the low- to high-Brig-Cluster from the sh-655 dataset (Thöle et al., in prep).

II) *S. antarctica* dominates during glacial maximum MIS 12

The assemblage of MIS 12 glacial maximum is dominated by *S. antarctica* reaching 60% around 437 ka. *Brigantedinium* spp. *Spiniferites* spp. and *S. nephroides* and *S. quanta* remain less than 10% in this assemblage. Noteworthy is the absence of *Spiniferites* spp., the only time in the downcore distribution. This assemblage can be associated with the Sant-Cluster, although the composition of the subspecies in this sample is somewhat different from the modern Sant-Cluster.

III) Transition from P- to G-dominance during Termination V

The glacial termination displays a transition from P- to G-dinocyst dominated assemblage, indicating a change in marine productivity. S. antarctica decreases to disappear at ca. 428 ka, while the assemblage increases in biodiversity. The assemblage appears most similar to low-Brig-Cluster with a variety of dinocysts reaching considerable abundances, including *Brigantedinium* spp. *I. pallidum*, *S. nephroides*, *S. quanta*, *I. minutum*, *Spiniferites* spp., *N. labyrinthus*.

IV) MIS 11c dominated by *N. labyrinthus*

The assemblage of MIS11c (415-398 ka) is dominated by *N. labyrinthus*; logically, the assemblage is assigned to the Nlab-Cluster. Other dinocysts present are S. quanta and Impagidinium spp. and in lesser abundance *I. pallidum*, *I. minutum*.

V) No clear dominance in the assemblage during the later stage of MIS11

The assemblage from the later stage of MIS 11 (< 400 ka; < 41.5 m CCSF-D) display a substantial decrease of both *N. labyrinthus* and no clear dominance of other dinocysts, except for *Spiniferites* spp., though *Spiniferites* spp. have been abundant in the entire downcore assemblage distribution.

5. Discussion

TEX_{86}-based SST estimates (~6-13 °C) are generally in correspondence with the temperature ranges from the modern-day clusters by Thöle et al. (in prep) that are assigned to the paleo-assemblages from U1534. However, there are two exceptions: namely the assemblage of MIS 12 assigned to the Sant-Cluster, and the high relative abundance of *Spiniferites* spp. that occur

throughout the assemblage. *Spiniferites* spp. dominance is suggestive of SST ~28 °C, much higher than found by TEX_{86}-baed SST.

5.1 Erosion and deposition under the SAF

An explanation for these biases could be sought from the transport factor. Due to the locality of Site U1534, it is suspected to be influenced by strong ocean currents, inducing lateral and meridional zonation due to the Falkland Current's south-to-north orientation. The clusters (Thöle et al. (in prep)) relate to key oceanic zones generally describing transitions in surface oceanographic conditions from pole to equator, with a quasi-latitudinal orientation. Additionally, the South Falkland Slope is expected to be influenced by Patagonian continental shelf waters, for which a strong SST temperature was described between the shelf water and the Falkland Current (see Section 2.1.1 Drake Passage Throughflow and the "cold water route"). Spiniferites spp. is suspected of partly being reworked due to its Paleogene-Holocene occurrence. Only during MIS 12 glacial maximum were *Spiniferites* spp. not present. It could point to decreased reworking during glacial phases due to decreased current action.

The presence of hiatuses and the high reworking are related to strong deep-water circulation, currents and eddies, shaping the sediment drift in the area (Howe et al., 1997; Nicholson & Stow, 2019). Indeed, large seabed erosion and scouring features have been revealed by seismic sections of the area (Fig. 9; Weber et al., 2019; Peck et al., 2021; Nicolson and Stow, 2019).

The entrance of the SAF into the Falkland Through via the narrow 54-54 Passage is linked to temporally elevated velocities and the formation of meso-scale eddies, with vortices extending down to the seabed (Hallberg & Gnanadesikan, 2006; Ito et al., 2010). The SAF-associated current reaches elevated velocities of >10 cm/s in its core extending from 1400 m, close to the pycnocline between AAIW and Upper Circumpolar Deep Water (UCDW), to 1800 m water depth (Nicholson & Stow, 2019). Such current strengths are suspected of causing erosion in the Falkland Through, where a thick Neogene sequence is present (Nicholson & Stow, 2019). This could hypothetically have caused Neogene specimens to be resuspended and mixed in the water column to ultimately become deposited higher up onto the South Falkland Slope Drift. Erosion could have occurred at any other location, as the area is generally subjected to high turbulence. Nevertheless, the reworked Neogene or Paleogene material must be analysed and identified to couple it with non-Pleistocene deposits from the region and trace their origin.

Ice rafting is another probable transport mechanism of reworked material into the area (Harland et al., 1999). Iceberg discharge was additionally contributed from the Patagonian Ice Sheet (Toyos et al., 2022), ending up in the ACC and transported into the South Atlantic. Iceberg discharge in the Atlantic section of the Southern Ocean mainly occurs via Iceberg Alley (Thöle et al., in prep). In the present-day ocean, Iceberg Alley is located south of the PF, to the southeast of Site U1534. It is debatable if the iceberg discharge had reached the Falkland Current during MIS 12 or Termination V. In the modern Southern Ocean, Iceberg Alley is associated with assemblages dominated by *I. minutum*, belonging to the Imin-cluster (Thöle et al., in prep.). Therefore, the most valid indication for Iceberg Alley reaching Site U1534 would be a resembling dinocyst assemblage to the Imin-cluster. Dinocysts associated with iceberg discharge (Imin-Cluster) may be expected at Termination V after MIS 12. Dinocysts associated with Imin-Cluster are present but not dominating in the assemblage. *I. minutum* is generally not majorly represented throughout the assemblage, indicating no direct presence of ice bergs in the Falkland Region.

5.2 Regional palaeoceanographic reconstruction for Site U1534

The SAF is expected to remain near its position in the Falkland Current due to the south-to-north orientation of the Falkland Current, concurred by the SST_{exp} of 6 and 13.5 °C that fits the sub-Antarctic zone. However, proximity between SAF and the PF may have changed on glacial-interglacial timescale, and changes in the strength of the Falkland Current, related to the strength of the ACC and functioning of the cold water route, are suggested to have resulted in the 'mirrored' SST_{exp} pattern, with colder SST during the interglacial MIS 11.

The reconstruction of the palaeoceanographic setting can be reduced to a simplistic view of four major intervals: I.) Preceding the glacial maximum of MIS 12; II.) the glacial maximum of MIS 12; III.) Termination V; the opening of the cold water route; IV.) the interglacial optimum of MIS11c and a well-functioning cold water route; and V.) the later stage of MIS 11 with reduced cold water route transport.

I) Preceding the glacial maximum of MIS 12

The climate preceding MIS 12 was intermediate: neither full-glacial nor interglacial. Intermediate was also dinocysts assemblage, which is assigned to low- to high-Brig-Cluster. The Brig-Clusters are not much restricted by environmental parameters. The High-Brig-cluster

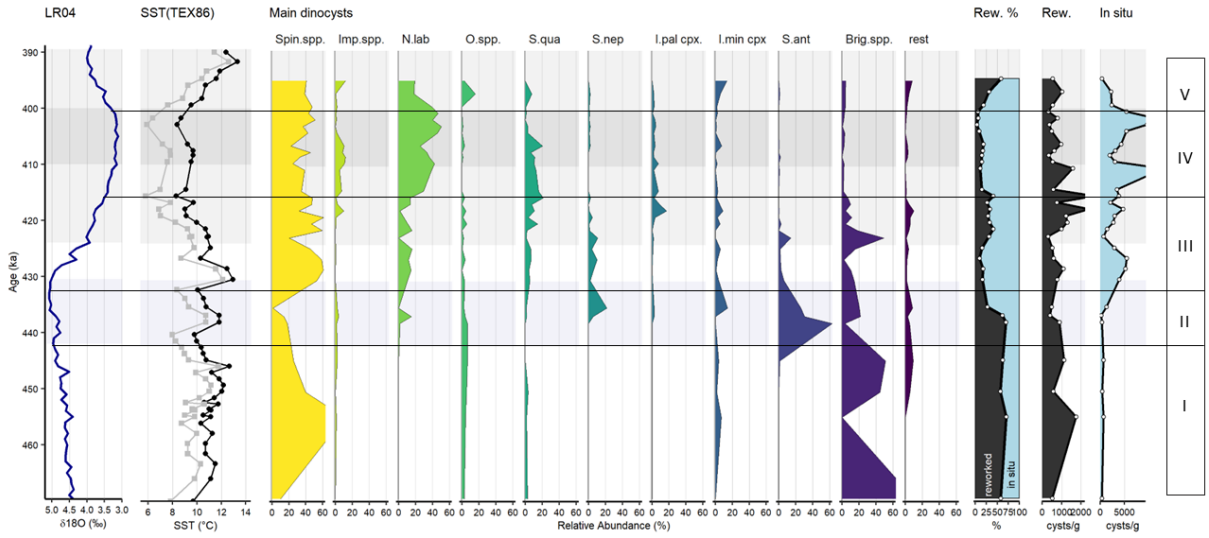

Figure 24. **TEX86-based SST reconstruction and the dinocyst assemblage distribution of U1534 togheterh with the LR04 stacked δ^{18}O record**. Glacial maximum MIS 12 (ca. 430 – 440 ka) is represented by the light blue area. MIS 11 (374 – 424 ka) is indicated by the light grey area, MIS 11c (400 – 410 ka) by the darker grey area. The roman numbers on the right are assigned to the distinctive phases as discussed in the text below.

is described to occur far to the south but also displays an affinity with coastal sites. Indeed, the modern Patagonian continental shelf contains a high relative abundance of *Brigantedinium* spp. I suggest that Patagonian shelf waters perturbated further onto the South Falkland Slope, resulting in moderately high SST values. The influence of the cold water route was likely reduced, inferring a weaker ACC and reduced mixing under the SAF.

II) Full-glacial MIS 12 and reduction of the cold water route

MIS 12 glacial maximum (~437 ka) is clearly reflected by dinocyst assemblage assigned to Sant-Cluster, which infers a northward PF migration and the Antarctic Zone extension. Sant-Cluster is typically present in cold SSTs of < 0 °C and may indicate the nearby presence of sea ice, though this is typical for sites closer to the Antarctic Continent. Sant-Cluster can also point towards cold SST and high nutrient concentrations, but with limited sea ice influence, indicative of the high-nutrient low-productivity (HNLP) signature from the AZ. The absence of high abundance of *I. minutum* cpx. in the assemblage suggests limited sea ice influence.

TEX_{86}-based SST estimates contradict the dinocyst assemblage interpretation, which remains (although ~1-2°C lower than preceding the glacial maximum) in the range typical for the SAZ. The relative warm SST estimates suggest a decreased functioning of the cold water route, as expected during glacial phases (See Section 1.3. Drake Passage throughflow and the "cold water route". A northern position of the SAF in the SE Pacific and Drake Passage, northward

extended sea ice, and reduced SWW wind forcing resulted in a more sluggish glacial Drake Passage throughflow of ACC, resulted in decreased cold water transport into the South Atlantic, and would also infer less vigorous dynamics SAF dynamics, such as reduced mixing (Fig. 25). The surface water at the South Falkland Slope is therefore expected to be increased stratified, with warmer Patagonian shelf water or SAMW resting on top, resulting in relative warm SST_{exp} values.

This bias between TEX86-based SST and the interpretation of Sant-Cluster suggests large SST gradients and may be overcome by the close or immediate proximity (effectively merging) of the SAF and PF in the Falkland Current (Orsi et al., 1995, Peterson and Whitworth, 1989). the SAF is restricted from migrating further north by the bathymetry of the North Scotia Ridge and the 54-54 Passage, therefore expected to remain in position in the Falkland Current. Glacial expansion likely induced the PF to migrate northward in the Scotia Sea, closing in on the SAF. Whether the PF has overcome bathymetric thresholds to cross the North Scotia Ridge through a passage more to the west of the Shaq Rock Passage (its current gateway into the Atlantic) is debatable, but possible. Meridional particle transport is expected to be responsible for introducing AZ-associated dinocyst assemblage (Sant-Cluster) into the contourite drift on the South Falkland Slope Drift.

III) Termination V - glacial termination and the opening of the cold water route

Termination V ended the glacial conditions, displayed by an initial SST increase of ~4°C from 435 ka to 428 ka. The onset of the southward migration of the SWW and Fronts is expected during this early stage of Termination V, but not enough to effectively open up the cold water route. Besides, sea ice is also still likely obstructing the Drake Passage. It is expected that the Drake Passage throughflow of ACC remained sluggish like during the glacial maximum, resulting in reduced cold water transport and low mixing dynamics under the SAF, allowing stratification, with the Patagonian shelf water, or SAMW, to rest on top of AAIW. Patagonian shelf water is expected to warm more during this first stage of global warming, resulting in elevated TEX86-based SST values. The biotic response was observed in a vanishing Sant-Cluster to become overtaken by a low-Brig-Cluster, reflecting the south-eastward migration of

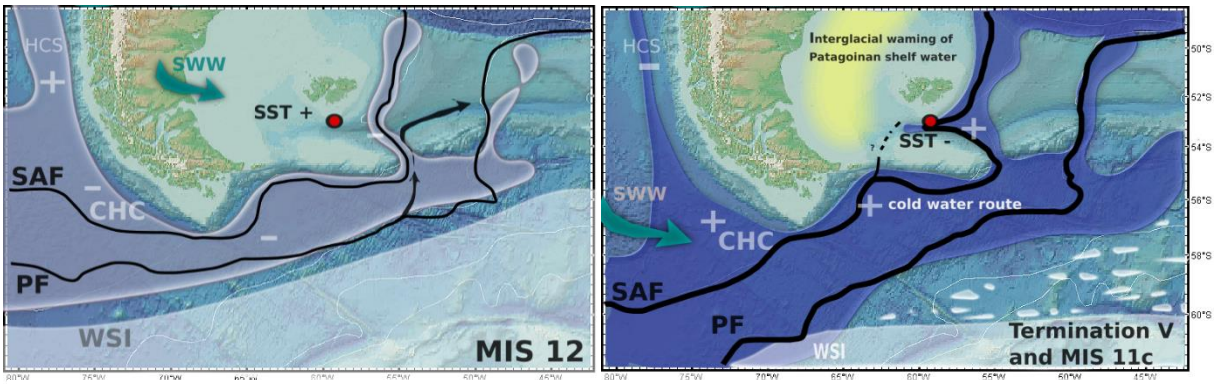

Figure 25. Interpretational maps for comparison between the cold water route at MIS12 glacial maximum and during Termination V into MIS 11c. (left) Drake Passage throughflow was more sluggish during MIS 12, due to northerly position of SAF and SWW, leading to enhanced bifurcation of ACC into the HCS; and reduced wind forcing on ACC, and obstruction by winter sea ice. (right) Opening of the cold water route during Termination V. is related to southward migration of SAF and SWW leading to enhanced ACC transport via CHC; retreating winter sea ice, and enhanced wind shear stresses. Increased cold water transport into the Falkland Region, while Patagonian shelf water heat during global warming likely resulted in stark SST gradients near the South Falkland Slope.

the PF, away from the Falkland Current and the broadening of the SAZ. The assemblage also transitioned from P- to G-dinocysts, concurring the LPHN Antarctic Zone to move away.

The later stage of Termination V (from ca. 428 to 415 ka) portrays the transition to interglacial conditions of MIS 11. TEX86-based SST displays a distinctive cooling trend from 13°C to a minimum of ~6°C and is interpreted as the opening up of the cold water route. SWW became increasingly aligned with the Drake Passage, shear stresses on the ACC became enhanced; southward migration of SAF resulted in less bifurcation of the Northern ACC branch and therefore more ACC transport to the Drake Passage, and the sea ice in the Drake Passage had withdrawn southwards, no longer forming a major obstruction. Hence, the cold water route effectively opened up (Fig. 25). Enhanced transport of cold subantarctic water into the Falkland Current, accompanied by strong SAF dynamics including mixing of cold water masses, perturbates strongly onto the South Falkland Slope and possibly further onto the Patagonian continental shelf.

The biotic response to the colder waters and SAF dynamics may be somewhat delayed. The low-Brig-Cluster can still be linked to shallow water influence from the continental slope, but high abundances of P-dinocysts may indicate colder, high productivity water.

IV) MIS 11c - optimal functioning of the cold water route

Full-interglacial conditions during MIS 11c (ca 415 to 400 ka) is associated with the fully functioning cold water route. Enhanced transport of cold subantarctic water into the Falkland Current, accompanied by strong SAF dynamics including mixing of cold water masses, perturbates strongly onto the South Falkland Slope, resulting in the low SST(TEX_{86}) values throughout the interglacial. The dinocyst assemblage was partly assigned to Nlab-Cluster, is indicative of relatively cold SST, and can strongly be associated with well-ventilated bottom waters indicating strong mixing under the SAF. Consistent with this interpretation is the increased water column overprint index. The index shows a similar trend to the decreasing SST, which may reflect deeper synthesised GDGTs due to the mixing of the water column. The Patagonian shelf waters would have warmed substantially during the interglacial optimum, suggesting strong SST gradient nearby the South Falkland Slope between the SAF and the warm water from the Patagonian continental shelf.

V) Weakening of the ACC at the later stage of MIS 11

The later stage of MIS 11, from 400 ka onwards, displayed an SST increase of ~7°C. Such amplitudes are typical for glacial-interglacial transition in the Southern Ocean but would have been expected during Termination V instead of ~30 kyr later. Thus, the SST warming appears to be delayed after the optimum of the interglacial. Global ice volume started to increase (See LR04 stack; Fig. 20), and the SWW were likely migrating slightly north, decreasing aligned with the Drake Passage. Consequently, a reduced cold water route resulted in reduced cold water input into the Falkland Current, and reduced ACC strength resulted in the decreased influence of the SAF onto the South Falkland Slope, allowing the increased influence of Patagonian Shelf water in the region.

6. Conclusions

This research aimed to unravel the palaeoceanographic setting of U1534 regarding the Subantarctic Front and the cold water route during MIS 12-11, based on a combining a marine palynological and an organic geochemical approach.

The *S. antarctica* dominated assemblage during MIS 12 suggests that a northward expansion of the Antarctic zone had expanded far north with respect to its current position, though it is expected that the SAF remained in position in the Falkland Current based on the relative high SST estimates. Termination V displays a notable change in oceanographic settings, with first a short warming of SST, after which a cooling trend is observed, pointing towards enhanced transport of cold, subantarctic water into the Falkland Region, and is strongly associated with the opening up of the cold water route and thus enhanced ACC transport through the Drake Passage. Enhanced ACC strength is also expected to induce stronger mixing, bringing colder water to the surface waters. Indeed, the SST estimates during MIS 11c (~6-8°C) are characteristic temperatures for the SAF. The dinocyst assemblage assigned to Nlab-Cluster displays the response to increased mixing of colder water under the SAF.

The low, relative stable SST remained throughout MIS 11c, indicating that the cold water route remained functional throughout the interglacial. The fact that SST warming occurred 30 kyr after Termination V and after the interglacial optimum indicates the dampening effect of the cold water route on interglacial warming. It is therefore concluded that the cold water route countered the global warming pattern, substantially cooling the region via the delivery of cold, pacific-sourced subantarctic water masses, including AAIW into the South Atlantic; and that only the sea water experienced warming of the interglacial due to reduced ACC transport through the Drake Passage, pointing out its clear importance in the climate system.

Acknowledgements

First of all, I would like to thank both Peter Bijl and Lena Thole for supervising me and giving me the opportunity to execute this research. I am particularly thankful to Lena for checking up on me, even after 10 pm when I was still online on Teams.

I would like to thank the staff members of the Utrecht Geo Lab for their assistance with the palynological and geochemical lab procedures.

I would like to thank Victoria Peck for her biostratigraphic work and for providing me with the biogeochemical tie-points, and I am particularly grateful for the fast responses on email to help me understand the matter.

I also would like to thank my roommates for all the diners cooked while I was hidden in my study cave. Especially Bram Loef and Thomas Brunekreef have my gratefulness for consuming the many litres of coffee together, as we were in the same boat.

I would like to thank my friend Bram for borrowing me his big additional screen monitor, which proved to be a major game changer in the writing and plotting saga of the past months.

And lastly, I would like to show my greatest gratitude to my girlfriend Misha, for lifting the spirit and keeping me going..

Data availability

Dinocyst counts, GDGT peak-integrations and R script are available upon request.

References

Ai, X. E., Studer, A. S., Sigman, D. M., Martínez-García, A., Fripiat, F., Thöle, L. M., Michel, E., Gottschalk, J., Arnold, L., Moretti, S., Schmitt, M., Oleynik, S., Jaccard, S. L., & Haug, G. H. (2020). Southern Ocean upwelling, Earth's obliquity, and glacial-interglacial atmospheric CO2 change. *Science*, *370*(6522), 1348–1352. https://doi.org/10.1126/SCIENCE.ABD2115/SUPPL_FILE/ABD2115_AI_SM.PDF

Anderson, R. F., Ali, S., Bradtmiller, L. I., Nielsen, S. H. H., Fleisher, M. Q., Anderson, B. E., & Burckle, L. H. (2009). Wind-driven upwelling in the southern ocean and the deglacial rise in atmospheric CO2. *Science*, *323*(5920), 1443–1448. https://doi.org/10.1126/SCIENCE.1167441/SUPPL_FILE/ANDERSON.SOM.PDF

Armour, K. C., Marshall, J., Scott, J. R., Donohoe, A., & Newsom, E. R. (2016). Southern Ocean warming delayed by circumpolar upwelling and equatorward transport. *Nature Geoscience 2016 9:7*, *9*(7), 549–554. https://doi.org/10.1038/NGEO2731

Bard, E., & Rickaby, R. E. M. (2009). Migration of the subtropical front as a modulator of glacial climate. *Nature 2009 460:7253*, *460*(7253), 380–383. https://doi.org/10.1038/nature08189

Bijl, P. K., Frieling, J., Cramwinckel, M. J., Boschman, C., Sluijs, A., & Peterse, F. (2021). *Maastrichtian-Rupelian paleoclimates in the southwest Pacific-a critical re-evaluation of biomarker paleothermometry and dinoflagellate cyst paleoecology at Ocean Drilling Program Site 1172*. *17*. https://doi.org/10.5194/cp-17-2393-2021

Bijl, P. K., Pross, J., Warnaar, J., Stickley, C. E., Huber, M., Guerstein, R., Houben, A. J. P., Sluijs, A., Visscher, H., Brinkhuis, H., Bijl, C. :, Pross, J., Warnaar, J., Stickley, C. E., Huber, M., Guerstein, R., Houben, A. J. P., Sluijs, A., Visscher, H., & Brinkhuis, H. (2011). Environmental forcings of Paleogene Southern Ocean dinoflagellate biogeography. *Paleoceanography*, *26*(1), 1202. https://doi.org/10.1029/2009PA001905

Blaga, C. I., Reichart, G. J., Heiri, O., & Sinninghe Damsté, J. S. (2009). Tetraether membrane lipid distributions in water-column particulate matter and sediments: A study of 47 European lakes along a north-south transect. *Journal of Paleolimnology*, *41*(3), 523–540. https://doi.org/10.1007/S10933-008-9242-2/FIGURES/7

Burke, A., & Robinson, L. F. (2012). The southern ocean's role in carbon exchange during the last deglaciation. *Science*, *335*(6068), 557–561. https://doi.org/10.1126/SCIENCE.1208163/SUPPL_FILE/BURKE.SOM.REV.PDF

Candy, I., Schreve, D. C., Sherriff, J., & Tye, G. J. (2014). Marine Isotope Stage 11: Palaeoclimates, palaeoenvironments and its role as an analogue for the current interglacial. *Earth-Science Reviews*, *128*, 18–51. https://doi.org/10.1016/j.earscirev.2013.09.006

Carme Huguet. (2007). *TEX86 paleothermometry : proxy validation and application in marine sediments*. https://www.researchgate.net/publication/27705641

Chapman, C. C., Lea, M. A., Meyer, A., Sallée, J. B., & Hindell, M. (2020). Defining Southern Ocean fronts and their influence on biological and physical processes in a changing

climate. *Nature Climate Change*, *10*(3), 209–219. https://doi.org/10.1038/S41558-020-0705-4

Cramwinckel, M. J., Huber, M., Kocken, I. J., Agnini, C., Bijl, P. K., Bohaty, S. M., Frieling, J., Goldner, A., Hilgen, F. J., Kip, E. L., Peterse, F., Van Der Ploeg, R., Röhl, U., Schouten, S., & Sluijs, A. (2018). Synchronous tropical and polar temperature evolution in the Eocene. *Nature 2018 559:7714*, *559*(7714), 382–386. https://doi.org/10.1038/S41586-018-0272-2

De Jonge, C., Radujković, D., Sigurdsson, B. D., Weedon, J. T., Janssens, I., & Peterse, F. (2019). Lipid biomarker temperature proxy responds to abrupt shift in the bacterial community composition in geothermally heated soils. *Organic Geochemistry*, *137*, 103897. https://doi.org/10.1016/J.ORGGEOCHEM.2019.07.006

Dearing Crampton-Flood, E., Tierney, J. E., Peterse, F., Kirkels, F. M. S. A., & Sinninghe Damsté, J. S. (2020). BayMBT: A Bayesian calibration model for branched glycerol dialkyl glycerol tetraethers in soils and peats. *Geochimica et Cosmochimica Acta*, *268*, 142–159. https://doi.org/10.1016/J.GCA.2019.09.043

Droxler, A., & Howard, W. R. (2003). *Unique and Exceptionally Long Interglacial Marine Isotope Stage 11: Window Into Earth Warm Future Climate*. https://doi.org/10.1029/137GM01

Esper, O., & Zonneveld, K. A. F. (2007a). *The potential of organic-walled dinoflagellate cysts for the reconstruction of past sea-surface conditions in the Southern Ocean*. https://doi.org/10.1016/j.marmicro.2007.07.002

Esper, O., & Zonneveld, K. A. F. (2007b). The potential of organic-walled dinoflagellate cysts for the reconstruction of past sea-surface conditions in the Southern Ocean. *Marine Micropaleontology*, *65*(3–4), 185–212. https://doi.org/10.1016/J.MARMICRO.2007.07.002

Ferrari, R., Jansen, M. F., Adkins, J. F., Burke, A., Stewart, A. L., & Thompson, A. F. (2014). *Antarctic sea ice control on ocean circulation in present and glacial climates*. *111*(24). https://doi.org/10.1073/pnas.1323922111

Fischer, H., Meissner, K. J., Mix, A. C., Abram, N. J., Austermann, J., Brovkin, V., Capron, E., Colombaroli, D., Daniau, A., Dyez, K. A., Felis, T., Finkelstein, S. A., Jaccard, S. L., Mcclymont, E. L., Rovere, A., Sutter, J., Wolff, E. W., Affolter, S., Bakker, P., … Sarnthein, M. (2018). *anthropogenic warming and beyond*. https://doi.org/10.1038/s41561-018-0146-0

Gruber, N., Landschützer, P., Landschützer, L., & Lovenduski, N. S. (2018). *The Variable Southern Ocean Carbon Sink*. https://doi.org/10.1146/annurev-marine-121916

H Weijers, J. W., H Lim, K. L., Aquilina, A., Sinninghe Damsté, J. S., Pancost, R. D., H Lim, K. L., Aquilina, A., Sinninghe Damsté, J. S., & Pancost, R. D. (2011). Biogeochemical controls on glycerol dialkyl glycerol tetraether lipid distributions in sediments characterized by diffusive methane flux. *Geochemistry, Geophysics, Geosystems*, *12*(10), 10010. https://doi.org/10.1029/2011GC003724

Hallberg, R., & Gnanadesikan, A. (2006). The Role of Eddies in Determining the Structure and Response of the Wind-Driven Southern Hemisphere Overturning: Results from the Modeling Eddies in the Southern Ocean (MESO) Project. *Journal of Physical Oceanography*, *36*(12), 2232–2252. https://doi.org/10.1175/JPO2980.1

Harland, R., & Pudsey, C. J. (1999). Dinoflagellate cysts from sediment traps deployed in the Bellingshausen, Weddell and Scotia seas, Antarctica. *Marine Micropaleontology*, *37*(2), 77–99. https://doi.org/10.1016/S0377-8398(99)00016-X

Hartman, J. D., Sangiorgi, F., Barcena, M. A., Tateo, F., Giglio, F., Albertazzi, S., Trincardi, F., Bijl, P. K., Langone, L., & Asioli, A. (2021). Sea-ice, primary productivity and ocean temperatures at the Antarctic marginal zone during late Pleistocene. *Quaternary Science Reviews*, *266*, 107069. https://doi.org/10.1016/J.QUASCIREV.2021.107069

Hodell, D. A., Charles, C. D., & Ninnemann, U. S. (2000). Comparison of interglacial stages in the South Atlantic sector of the Southern Ocean for the past 450 kyr: Implications for Marine Isotope Stage (MIS) 11. *Global and Planetary Change*, *24*(1), 7–26. https://doi.org/10.1016/S0921-8181(99)00069-7

Hoem, F. S., Sauermilch, I., Hou, S., Brinkhuis, H., Sangiorgi, F., & Bijl, P. K. (2021). *Late Eocene-early Miocene evolution of the southern Australian subtropical front: a marine palynological approach*. *40*, 175–193. https://doi.org/10.5194/jm-40-175-2021

Hopmans, E. C., Weijers, J. W. H., Schefuß, E., Herfort, L., Sinninghe Damsté, J. S., & Schouten, S. (2004). A novel proxy for terrestrial organic matter in sediments based on branched and isoprenoid tetraether lipids. *Earth and Planetary Science Letters*, *224*(1–2), 107–116. https://doi.org/10.1016/J.EPSL.2004.05.012

Howe, J. A., Pudsey, C. J., & Cunningham, A. P. (1997). Pliocene-Holocene contourite deposition under the Antarctic Circumpolar Current, Western Falkland Trough, South Atlantic Ocean. *Marine Geology*, *138*, 27–50.

Ito, T., Woloszyn, M., & Mazloff, M. (2010). Anthropogenic carbon dioxide transport in the Southern Ocean driven by Ekman flow. *Nature 2010 463:7277*, *463*(7277), 80–83. https://doi.org/10.1038/NATURE08687

Jaccard, S. L., Hayes, C. T., Hodell, D. A., Anderson, R. F., Sigman, D. M., & Haug, G. H. (2012). *Two Modes of Change in Southern Ocean Productivity Over the Past Million Years*. *219*(2009).

Kim, J. H., van der Meer, J., Schouten, S., Helmke, P., Willmott, V., Sangiorgi, F., Koç, N., Hopmans, E. C., & Damsté, J. S. S. (2010). New indices and calibrations derived from the distribution of crenarchaeal isoprenoid tetraether lipids: Implications for past sea surface temperature reconstructions. *Geochimica et Cosmochimica Acta*, *74*(16), 4639–4654. https://doi.org/10.1016/J.GCA.2010.05.027

Kohfeld, K. E., & Chase, Z. (2017). Temporal evolution of mechanisms controlling ocean carbon uptake during the last glacial cycle. *Earth and Planetary Science Letters*, *472*, 206–215. https://doi.org/10.1016/J.EPSL.2017.05.015

Lamy, F., Arz, H. W., Kilian, R., Lange, C. B., Lembke-jene, L., Wengler, M., & Kaiser, J. (2015). *Glacial reduction and millennial-scale variations in Drake Passage throughflow*. *112*(44), 13496–13501. https://doi.org/10.1073/pnas.1509203112

Le Quéré, C., Rödenbeck, C., Buitenhuis, E. T., Conway, T. J., Langenfelds, R., Gomez, A., Labuschagne, C., Ramonet, M., Nakazawa, T., Metzl, N., Gillett, N., & Heimann, M. (2007). Saturation of the southern ocean CO2 sink due to recent climate change. *Science*,

316(5832), 1735–1738. https://doi.org/10.1126/SCIENCE.1136188/SUPPL_FILE/LE_QUERE_SOM.PDF

Lisiecki, L. E., & Raymo, M. E. (2005). A Pliocene-Pleistocene stack of 57 globally distributed benthic δ18O records. *Paleoceanography*, *20*(1), 1–17. https://doi.org/10.1029/2004PA001071

Marret, F., Bradley, L., Vernal, A. De, Hardy, W., Kim, S., Mudie, P., Penaud, A., Pospelova, V., Price, A. M., Radi, T., & Rochon, A. (2019). Marine Micropaleontology From bi-polar to regional distribution of modern dinoflagellate cysts , an overview of their biogeography. *Marine Micropaleontology*, *February*, 101753. https://doi.org/10.1016/j.marmicro.2019.101753

Marret, F., & Zonneveld, K. A. F. (2003). Atlas of modern organic-walled dinoflagellate cyst distribution. *Review of Palaeobotany and Palynology*, *125*(1–2), 1–200. https://doi.org/10.1016/S0034-6667(02)00229-4

Marshall, J., & Speer, K. (2012). Closure of the meridional overturning circulation through Southern Ocean upwelling. *Nature Geoscience 2012 5:3*, *5*(3), 171–180. https://doi.org/10.1038/NGEO1391

Mazaud, A., Michel, E., Dewilde, F., & Turon, J. L. (2010). Variations of the Antarctic Circumpolar Current intensity during the past 500 ka. *Geochemistry, Geophysics, Geosystems*, *11*(8), 8007. https://doi.org/10.1029/2010GC003033

McClymont, E. L., Elmore, A. C., Kender, S., Leng, M. J., Greaves, M., & Elderfield, H. (2016). Pliocene-Pleistocene evolution of sea surface and intermediate water temperatures from the southwest Pacific. *Paleoceanography*, *31*(6), 895–913. https://doi.org/10.1002/2016PA002954

Michael E. Weber, Maureen E. Raymo, Victoria L. Peck, T. W. (2019). International Ocean Discovery Program Expedition 382 Preliminary Report Iceberg Alley and Subantarctic Ice and Ocean Dynamics. *Integrated Ocean Drilling Program: Preliminary Reports*, *366*, 1–40.

Naafs, B. D. A., Rohrssen, M., Inglis, G. N., Lähteenoja, O., Feakins, S. J., Collinson, M. E., Kennedy, E. M., Singh, P. K., Singh, M. P., Lunt, D. J., & Pancost, R. D. (2018). High temperatures in the terrestrial mid-latitudes during the early Palaeogene. *Nature Geoscience 2018 11:10*, *11*(10), 766–771. https://doi.org/10.1038/s41561-018-0199-0

Nicholson, U., & Stow, D. (2019). Erosion and deposition beneath the Subantarctic Front since the Early Oligocene. *Scientific Reports 2019 9:1*, *9*(1), 1–9. https://doi.org/10.1038/S41598-019-45815-7

O'Brien, C. L., Robinson, S. A., Pancost, R. D., Sinninghe Damsté, J. S., Schouten, S., Lunt, D. J., Alsenz, H., Bornemann, A., Bottini, C., Brassell, S. C., Farnsworth, A., Forster, A., Huber, B. T., Inglis, G. N., Jenkyns, H. C., Linnert, C., Littler, K., Markwick, P., McAnena, A., … Wrobel, N. E. (2017). Cretaceous sea-surface temperature evolution: Constraints from TEX86 and planktonic foraminiferal oxygen isotopes. *Earth-Science Reviews*, *172*, 224–247. https://doi.org/10.1016/J.EARSCIREV.2017.07.012

Orsi, A H, Johnson, G. C., & Bullister, J. L. (1999). Circulation, mixing, and production of

Antarctic Bottom Water. *Progress in Oceanography*, *43*, 55–109.

Orsi, Alejandro H., Whitworth, T., & Nowlin, W. D. (1995). On the meridional extent and fronts of the Antarctic Circumpolar Current. *Deep Sea Research Part I: Oceanographic Research Papers*, *42*(5), 641–673. https://doi.org/10.1016/0967-0637(95)00021-W

Peck, V. L., Weber, M. E., Raymo, M. E., Williams, T. V. L., Williams, T., Armbrecht, L. H., Bailey, I., Brachfeld, S. A., Cardillo, F. G., Du, Z., Fauth, G., García, M., Glüder, A., Guitard, M. E., Gutjahr, M., Hemming, S. R., Hernández-Almeida, I., Hoem, F. S., Hwang, J.-H., … Zheng, X. (2021). Site U1534 1. *Expedition*, *382*. https://doi.org/10.14379/iodp.proc.382.103.2021

Pérez, L. F., Hernández-Molina, F. J., Esteban, F. D., Tassone, A., Piola, A. R., Maldonado, A., Preu, B., Violante, R. A., & Lodolo, E. (2015). Erosional and depositional contourite features at the transition between the western Scotia Sea and southern South Atlantic Ocean: links with regional water-mass circulation since the Middle Miocene. *Geo-Marine Letters*, *35*(4), 271–288. https://doi.org/10.1007/S00367-015-0406-6/TABLES/2

Pérez, L. F., Martos, Y. M., García, M., Weber, M. E., Raymo, M. E., Williams, T., Bohoyo, F., Armbrecht, L., Bailey, I., Brachfeld, S., Glüder, A., Guitard, M., Gutjahr, M., Hemming, S., Hernández-Almeida, I., Hoem, F. S., Kato, Y., O'Connell, S., Peck, V. L., … Zheng, X. (2021). Miocene to present oceanographic variability in the Scotia Sea and Antarctic ice sheets dynamics: Insight from revised seismic-stratigraphy following IODP Expedition 382. *Earth and Planetary Science Letters*, *553*, 116657. https://doi.org/10.1016/J.EPSL.2020.116657

Piola, A. R., Martínez Avellaneda, N., Guerrero, R. A., Jardón, F. P., Palma, E. D., & Romero, S. I. (2010). Malvinas-slope water intrusions on the northern Patagonia continental shelf. *Ocean Science*, *6*(1), 345–359. https://doi.org/10.5194/OS-6-345-2010

Prebble, J. G., Crouch, E. M., Carter, L., Cortese, G., Bostock, H., & Neil, H. (2013). Marine Micropaleontology An expanded modern dino fl agellate cyst dataset for the Southwest Paci fi c and Southern Hemisphere with environmental associations. *Marine Micropaleontology*, *101*, 33–48. https://doi.org/10.1016/j.marmicro.2013.04.004

Rühs, S., Schwarzkopf, F. U., Speich, S., & Biastoch, A. (2019). Cold vs. warm water route-sources for the upper limb of the Atlantic Meridional Overturning Circulation revisited in a high-resolution ocean model. *Ocean Science*, *15*(3), 489–512. https://doi.org/10.5194/OS-15-489-2019

Saavedra-Pellitero, M., Baumann, K. H., Lamy, F., & Köhler, P. (2017). Coccolithophore variability across Marine Isotope Stage 11 in the Pacific sector of the Southern Ocean and its potential impact on the carbon cycle. *Paleoceanography*, *32*(8), 864–880. https://doi.org/10.1002/2017PA003156

Sabine, C. L., Feely, R. A., Gruber, N., Key, R. M., Lee, K., Bullister, J. L., Wanninkhof, R., Wong, C. S., Wallace, D. W. R., Tilbrook, B., Millero, F. J., Peng, T. H., Kozyr, A., Ono, T., & Rios, A. F. (2004). The oceanic sink for anthropogenic CO2. *Science*, *305*(5682), 367–371. https://doi.org/10.1126/SCIENCE.1097403/SUPPL_FILE/SABINE.SOM.PDF

Sangiorgi, F., Bijl, P. K., Passchier, S., Salzmann, U., Schouten, S., McKay, R., Cody, R. D.,

Pross, J., Van De Flierdt, T., Bohaty, S. M., Levy, R., Williams, T., Escutia, C., & Brinkhuis, H. (2018). Southern Ocean warming and Wilkes Land ice sheet retreat during the mid-Miocene. *Nature Communications 2018 9:1*, *9*(1), 1–11. https://doi.org/10.1038/s41467-017-02609-7

Schouten, S., Hopmans, E. C., Schefuß, E., & Sinninghe Damsté, J. S. (2002). Distributional variations in marine crenarchaeotal membrane lipids: a new tool for reconstructing ancient sea water temperatures? *Earth and Planetary Science Letters*, *204*(1–2), 265–274. https://doi.org/10.1016/S0012-821X(02)00979-2

Schouten, S., Hopmans, E. C., & Sinninghe Damsté, J. S. (2013). The organic geochemistry of glycerol dialkyl glycerol tetraether lipids: A review. *Organic Geochemistry*, *54*, 19–61. https://doi.org/10.1016/J.ORGGEOCHEM.2012.09.006

Shi, J. R., Xie, S. P., & Talley, L. D. (2018). Evolving Relative Importance of the Southern Ocean and North Atlantic in Anthropogenic Ocean Heat Uptake. *Journal of Climate*, *31*(18), 7459–7479. https://doi.org/10.1175/JCLI-D-18-0170.1

Sigman, D. M., Hain, M. P., & Haug, G. H. (2010). atmospheric CO 2 concentration. *Nature*, *466*(7302), 47–55. https://doi.org/10.1038/nature09149

Smith, I. J., Stevens, D. P., Heywood, K. J., & Meredith, M. P. (n.d.). *Personal revised version of: Deep-Sea Research I*. *57*, 14–28. https://doi.org/10.1016/j.dsr.2009.10.010

Smith, I. J., Stevens, D. P., Heywood, K. J., & Meredith, M. P. (2010). The flow of the Antarctic Circumpolar Current over the North Scotia Ridge. *Deep Sea Research Part I: Oceanographic Research Papers*, *57*(1), 14–28. https://doi.org/10.1016/j.dsr.2009.10.010

Taylor, K. W. R., Huber, M., Hollis, C. J., Hernandez-Sanchez, M. T., & Pancost, R. D. (2013). *Re-evaluating modern and Palaeogene GDGT distributions: Implications for SST reconstructions*. https://doi.org/10.1016/j.gloplacha.2013.06.011

Thöle, L. M., Nooteboom, P. D., Hou, S, Wang, R, Nie, S., Michel, E., Sauermilch, I., Marret. F., Sangiorgi, F.,1, Peter K. Bijl, P. K., (in preparation). An expanded database of Southern Hemisphere surface sediment dinoflagellate cysts and their oceanographic affinities.

Toggweiler, J. R. (2009). Shifting westerlies. *Science*, *323*(5920), 1434–1435. https://doi.org/10.1126/SCIENCE.1169823/ASSET/D6FEED57-99B8-4EA0-A734-0243ADEB50BE/ASSETS/GRAPHIC/1434-1.GIF

Toyos, M. H., Lamy, F., Lange, C. B., Lembke-Jene, L., Saavedra-Pellitero, M., Esper, O., & Arz, H. W. (2020). Antarctic Circumpolar Current Dynamics at the Pacific Entrance to the Drake Passage Over the Past 1.3 Million Years. *Paleoceanography and Paleoclimatology*, *35*(7), e2019PA003773. https://doi.org/10.1029/2019PA003773

Toyos, M. H., Winckler, G., Arz, H. W., Lembke-Jene, L., Lange, C. B., Kuhn, G., & Lamy, F. (2022a). *Variations in export production, lithogenic sediment transport and iron fertilization in the Pacific sector of the Drake Passage over the past 400 ka*. https://doi.org/10.5194/cp-2021-85

Toyos, M. H., Winckler, G., Arz, H. W., Lembke-Jene, L., Lange, C. B., Kuhn, G., & Lamy, F. (2022b). Variations in export production, lithogenic sediment transport and iron

fertilization in the Pacific sector of the Drake Passage over the past 400gkyr. *Climate of the Past*, *18*(1), 147–166. https://doi.org/10.5194/CP-18-147-2022

Voigt, I., Chiessi, C. M., Piola, A. R., & Henrich, R. (2016). *Holocene changes in Antarctic Intermediate Water flow strength in the Southwest Atlantic*. https://doi.org/10.1016/j.palaeo.2016.09.018

Wanner, H., Beer, J., Bütikofer, J., Crowley, T. J., Cubasch, U., Flückiger, J., Goosse, H., Grosjean, M., Joos, F., Kaplan, J. O., Küttel, M., Müller, S. A., Prentice, I. C., Solomina, O., Stocker, T. F., Tarasov, P., Wagner, M., & Widmann, M. (2008). Mid- to Late Holocene climate change: an overview. *Quaternary Science Reviews*, *27*(19–20), 1791–1828.

Weber, M E, Raymo, M. E., Peck, V. L., Williams, T., Armbrecht, L. H., Bailey, I., Brachfeld, S. A., Cardillo, F. G., Du, Z., Fauth, G., García, M., Glüder, A., Guitard, M. E., Gutjahr, M., Hemming, S. R., Hernández-Almeida, I., Hoem, F. S., Hwang, J.-H., Iizuka, M., … Zheng, X. (2021). Expedition 382 methods. *Expedition*, *382*. https://doi.org/10.14379/iodp.proc.382.102.2021

Weber, Michael E, & Raymo, M. E. (2018). *International Ocean Discovery Program Expedition 382 Scientific Prospectus Iceberg Alley and South Falkland Slope Ice and Ocean Dynamics*. https://doi.org/10.14379/iodp.sp.382.2018

Williams, G., Brinkhuis, H., Pearce, M., Fensome, R., & Weegink, J. (2004). *5. SOUTHERN OCEAN AND GLOBAL DINOFLAGELLATE CYST EVENTS COMPARED: INDEX EVENTS FOR THE LATE CRETACEOUS-NEOGENE 1*. *189*.

Williams, T. J., Hillenbrand, C. D., Piotrowski, A. M., Allen, C. S., Frederichs, T., Smith, J. A., Ehrmann, W., & Hodell, D. A. (2019). Paleocirculation and Ventilation History of Southern Ocean Sourced Deep Water Masses During the Last 800,000 Years. *Paleoceanography and Paleoclimatology*, *34*(5), 833–852. https://doi.org/10.1029/2018PA003472

Wolff, E. W., Barbante, C., Becagli, S., Bigler, M., Boutron, C. F., Castellano, E., De Angelis, M., Federer, U., Fischer, H., Fundel, F., Hansson, M., Hutterli, M., Jonsell, U., Karlin, T., Kaufmann, P., Lambert, F., Littot, G. C., Mulvaney, R., Rö Thlisberger, R., … Wegner, A. (n.d.). *Changes in environment over the last 800,000 years from chemical analysis of the EPICA Dome C ice core*. https://doi.org/10.1016/j.quascirev.2009.06.013

Zhang, Y. G., Pagani, M., & Wang, Z. (2016). Ring Index: A new strategy to evaluate the integrity of TEX86 paleothermometry. *Paleoceanography*, *31*(2), 220–232. https://doi.org/10.1002/2015PA002848

Zhang, Y. G., Zhang, C. L., Liu, X.-L., Li, L., Hinrichs, K.-U., & Noakes, J. E. (2011). *Methane Index: A tetraether archaeal lipid biomarker indicator for detecting the instability of marine gas hydrates*. https://doi.org/10.1016/j.epsl.2011.05.031

.

Supplements

Appendix I. IODP Expedition 382 Site U1534A data

Sample	Expedition	Site	Hole	Core	Core type	section	Depth interval (cm)	Depth m.b.s.f.	Depth CCSF (m)	Tie-point (ka)	Age (ka)	$SST_{lin}(TEX_{86})$ (°C)	Dinocysts counted
									39.05	*344.5*			
TV1	382	1534	A	5	H	3	136-138	36.36	39.05	*390*	390.00	12.37373	0
TV2	382	1534	A	5	H	4	16-18	36.67	39.36		391.71	13.32348	0
TV3	382	1534	A	5	H	4	46-48	36.97	39.66		393.37	11.8824	0
									39.77	394			
TV4	382	1534	A	5	H	4	76-78	37.27	39.96		394.72	11.57499	74
TV5	382	1534	A	5	H	4	106-108	37.57	40.26		395.88	10.71137	0
TV6	382	1534	A	5	H	4	136-138	37.87	40.56		397.04		224
TV7	382	1534	A	5	H	5	16-18	38.17	40.86		398.20	10.4096	0
TV8	382	1534	A	5	H	5	46-48	38.47	41.16		399.36	9.536893	200
TV9	382	1534	A	5	H	5	76-78	38.77	41.46		400.53		254
TV10	382	1534	A	5	H	5	106-108	39.07	41.76		401.69	8.687714	227
TV11	382	1534	A	5	H	5	136-138	39.37	42.06		402.85	8.378766	231
TV12	382	1534	A	5	H	6	16-18	39.67	42.36		404.01		289
TV13	382	1534	A	5	H	6	76-78	40.27	42.96		406.33	9.232093	221
TV14	382	1534	A	5	H	6	106-108	40.57	43.26		407.50	9.677247	273
TV15	382	1534	A	5	H	7	16-18	40.78	43.47		408.31	9.694852	243
TV16	382	1534	A	5	H	7	46-48	41.08	43.77		409.47	9.516883	259
TV17	382	1534	A	5	H	7	76-78	41.38	44.07		410.63		258
TV18	382	1534	A	6	H	1	16-18	41.66	45.03		414.38	9.108494	301
TV19	382	1534	A	6	H	1	46-48	41.96	45.33		415.54	8.303305	285
TV20	382	1534	A	6	H	1	76-78	42.26	45.63		416.70	9.700926	214
TV21	382	1534	A	6	H	1	106-108	42.56	45.93		417.86	9.027003	269
TV22	382	1534	A	6	H	1	136-138	42.86	46.23		419.03	9.118009	250
TV23	382	1534	A	6	H	2	16-18	43.16	46.53		420.19	9.977827	211
TV24	382	1534	A	6	H	2	46-48	43.46	46.83		421.35	10.69482	121
									47.00	422			
TV25	382	1534	A	6	H	2	74-76	43.74	47.11		422.70	10.9441	112
TV26	382	1534	A	6	H	2	76-78	43.76	47.13		422.83	10.82933	0
TV27	382	1534	A	6	H	2	106-108	44.06	47.43		424.70	11.09558	215
TV28	382	1534	A	6	H	2	136-138	44.36	47.73		426.58	10.3074	234
TV29	382	1534	A	6	H	3	16-18	44.66	48.03		428.45	12.46813	211
TV30	382	1534	A	6	H	3	46-48	44.96	48.33		430.33	12.9367	256
									48.60	*432*			
TV31	382	1534	A	6	H	3	76-78	45.26	48.63		432.16	10.05871	0

TV32	382	1534	A	6	H	3	106-108	45.56	48.93		433.68	10.54251	0
TV33	382	1534	A	6	H	3	136-138	45.86	49.23		435.19	10.7647	84
TV34	382	1534	A	6	H	4	16-18	46.16	49.53		436.71	11.82484	79
									49.59	437			
TV35	382	1534	A	6	H	4	46-48	46.46	49.83		437.90	11.82257	60
TV35.1	382	1534	A	6	H	4	76-78	46.76	50.13		439.02		0
TV36	382	1534	A	6	H	4	106-108	47.06	50.43		440.14	9.796753	0
TV37	382	1534	A	6	H	4	136-138	47.36	50.73		441.26	9.988569	0
TV38	382	1534	A	6	H	5	16-18	47.66	51.03		442.37	10.35213	0
TV39	382	1534	A	6	H	5	46-48	47.96	51.33		443.49	10.51255	0
TV40	382	1534	A	6	H	5	76-78	48.26	51.63		444.61	10.75545	78
TV41	382	1534	A	6	H	5	106-108	48.56	51.93		445.73	12.64171	0
TV42	382	1534	A	6	H	5	136-138	48.86	52.23		446.85	11.20001	0
TV43	382	1534	A	6	H	6	16-18	49.16	52.53		447.96	11.82101	0
TV44	382	1534	A	6	H	6	46-48	49.46	52.83		449.08	12.1654	0
TV45	382	1534	A	6	H	6	76-78	49.76	53.13		450.20	12.04831	58
TV46	382	1534	A	6	H	6	106-108	50.06	53.43		451.32	11.41987	0
TV47	382	1534	A	6	H	6	136-138	50.36	53.73		452.44	11.74856	0
TV48	382	1534	A	6	H	7	16-18	50.66	54.03		453.55	11.14658	0
TV49	382	1534	A	6	H	7	46-48	50.96	54.33		454.67	11.13613	70
TV50	382	1534	A	7	H	1	16-18	51.16	53.66		452.18	10.5869	0
TV51	382	1534	A	7	H	1	46-48	51.46	53.97		453.33	10.98636	0
TV52	382	1534	A	7	H	1	76-78	51.76	54.26		454.41	10.52482	0
									54.42	*455*			
TV53	382	1534	A	7	H	1	106-108	52.06	54.56		455.85	10.33722	0
TV54	382	1534	A	7	H	1	136-138	52.36	54.86		457.65	11.25921	0
TV55	382	1534	A	7	H	2	16-18	52.66	55.16		459.45	10.69992	0
TV56	382	1534	A	7	H	2	46-48	52.96	55.46		461.25	10.70884	0
TV57	382	1534	A	7	H	2	76-78	53.26	55.76		463.05	11.507	0
									55.92	*464*			
TV58	382	1534	A	7	H	2	106-108	53.56	56.06		465.67	11.12552	0
TV59	382	1534	A	7	H	2	136-138	53.86	56.36		466.68	9.696573	40
TV60	382	1534	A	7	H	3	46-48	54.46	56.96		467.22	11.29837	0
									57.54	*483*			
									58.73	*493*			

Tie-points with italic font are added for the purpose of this study, all other tie-points were provided by V. Peck (2021).

Appendix II. Dinoflagellate cysts and their modern ecological affinities.

Dinocysts	**Occurrence & Biogeographic affinity**		Reference
Spiniferitus ramosus	Cosmopolitan; sub-polar to equatorial distribution; mostly restricted by the PF	Greatest abundance within or north of the STF; although present at either sides; high absolute abundances in high productivity areas, such as upwelling regions (or river discharge areas); can also occur in oligotrophic parts of open ocean, but more common in more shore-proximal settings; abundant when little competition is present; temperate regions; also tolerant of (permanently or seasonally) reduced upper water salinity due to river discharge or snow/ice melt.	Brinkhuis 1994; Prebble et al., 2013; Zonneveld et al., 2013;
Spiniferitus mirabilis *Achomospheara*	Temperate to equatorial distribution; present either side of the STF; (Zonneveld: STF roughly forming its southern boundaries)	Present in coastal as well in open oceanic environments; high relative abundances in reduced salinity (either seasonally or throughout the year); oligotrophic to eutrophic, with anoxic to well-ventilated bottom waters; present, though not typically abundant in all major upwelling areas; highest abundance (up to 78%) in areas including the Southern Atlantic Ocean within or north of the STF, at around 30-40° S.	Prebble et al., 2013; Zonneveld et al., 2013;
Spiniferitus bentorri	Temperate to equatorial, mainly coastal distribution	Highest relative abundances in (seasonally) mesotrophic to eutrophic settings, such as upwelling areas (with large inter-annual variability in the upper water's trophic state); can be abundant in oligotrophic regions, where large inter-annual variability in the trophic state of the upper waters can occur.	Prebble et al., 2013; Zonneveld et al., 2013;
Nematosphaeropsis labyrinthus	Cosmopolitan; full-marine eutrophic to oligotrophic environments, mainly south of the STF	Tolerant of most full-marine environmental conditions; can be abundant in SSTs <0 – >25°C in all seasons; though most abundant (>50%, up to 78%) observed in eutrophic environments with well-ventilated bottom waters, including the Southern Ocean; with > 40% relative abundance south of the STF.	Prebble et al., 2013; Zonneveld et al., 2013;
Impagidinium spp. (including *I. aculeatum, I. sphaericum, (I. paradoxum, etc).* excluding *I. pallidum)*	Present either side of the STF; also present south of the SAF	Open ocean; warmer water; highest abundance beneath STF	Prebble et al., 2013; Zonneveld et al., 2013;
Operculodinium spp. & I. Acueatum?	Cosmopolitan species, mainly present north of the STF	Open ocean	Frieling and Sluijs 2018; Pross and Brinkhuis 2005; Zonneveld et al., 2013
Brigantedinium spp.	Cosmopolitan; (high nutrient availability)	Highest abundance (>50%) beneath (?, or south) the STF, but can dominate from coastal regions to the central parts of the oceans, covering all ranges environmental gradients.	

Selenopemphix nephroides,	Temperate to equatorial regions; upwelling areas; high nutrient availability	(Highest abundance beneath STF, in same setting as Brigantedinium spp.(?) (Prebble); Highest rel. abundances (up to 14%) in upwelling areas with well-ventilated bottom waters, with large inter-annual trophic variability (mesotrophic to eutrophic).	Bijl et al., 2018; Frieling and Sluijs 2018; Prebble et al., 2013; Pross and Brinkman 2005; Sluijs, Pross and Brinkman 2005; Zonneveld et al., 2013
Selenopemphix quanta, *Echnidinium* spp.	Polar to equatorward distribution; upwelling areas, discharge plumes and frontal systems; high nutrient availability	Highest abundance beneath STF. Also high abundances (up to 44%), and generally restricted to eutrophic regions with high sea surface chlorophyll-a concentrations, including upwelling areas and fronts and discharge plumes; large inter-annual trophic variability; ventilated bottom waters.	Prebble et al., 2013; Zonneveld et al., 2013;
Islandinium minutum	Temperate to polar distribution; low salinity	Highest relative abundances in polar regions where SSTs do not exceed 0°C in winter; high abundance in regions with large seasonality with reduced water salinity due to ice melt; high nutrient - low productivity regions.	Zonneveld et al., 2013;
Dellala chatamensis	Temperate to polar distribution	Similar to I. pallidum, but a bit more temperate	Prebble et al., 2013
Impagidenium pallidum	Polar species; largely restricted to the south of the STF	Highest relative abundance (up to 39%) in [arctic and Antarctic] polar waters and in the vicinity of the polar fronts; relative abundance of >20% is indicates SSTs between -1.7 – 5.4 degrees (winter – summer); high [P] and [N] but low Cl-a concentrations in upper waters; well-ventilated bottom waters; indication for sea ice production/transport (reduced salinities).	Prebble et al., 2013; Zonneveld et al., 2013
Selenopemphix antarctica	polar species endemic to the southern oceans; restricted by the south of the STF.	Abundances > 20% occur south of the PF, where SST < 0 (winter, spring) up to 10 °C (summer). Not recorded near seasonal melting of ice. Typical present in "high nutrient/low chlorophyll" environments with well-ventilated bottom waters.	Prebble et al., 2013; Zonneveld et al., 2013.
Precingular gonyaulacoid cysts*:* *Bitectatodinium* *Filispaera* *Habibacysta* *Pyxidinopsis*	Outer shelf offshore		Frieling and Sluijs 2018; Pross and Brinkman 2005; Sluijs, Pross and Brinkman 2005

Appendix III. Clusters from reference datasets

K-mean cluster analysis by Prebble et al. (2013) has provided a classification of modern dinocyst assemblages for the Southern Hemisphere (dataset SH-311), although the study was mainly focussed on the SW Pacific region (dataset NZ-98). Three clusters were proposed for the Southern Hemisphere to occupy distinct ecological niches. Cluster 1 is dominated by S. antarctica and belongs to Polar waters. Cluster 2 was characterized by relative low-diversity assemblages dominated by *Brigantedinium* spp. and other peridinioid genera, associated with cool, temperate and high productivity waters. Cluster 7 contained high relative abundances of *O. centrocarpum* and was only observed in the South Atlantic samples. The tropical setting was characterized by sparse assemblage dominated by *Impagidinium* spp. High latitude settings were characterized by assemblages being too sparse to achieve thorough census counts, but with main components *I. pallidum*, *S. antarctica*, *Brigantedinium* spp. and *N. labyrinthus*. Largely restricted to the south of the STF were three taxa identified: *S. antarctica*, *D. chathamensis*, *I. pallidum*. However, *D. chathamensis* does appear north of the STF in other places in the SH. Four clusters were proposed to be linked to distinct biogeographic provinces in the SW-Pacific, based on k-means clustering of the NZ-98 dataset, but may be compared to other SH assemblages. Cluster 3 is dominated by *N. labyrinthus* and occurs in the SAW(?) south of the STF; Cluster 4 is dominated by *Brigantedinium* spp., *S. quanta* and *Echnidinium* spp. and are found near the STF and near shore sites; Cluster 5 is dominated by *O. centrocarpum*, *S. ramosus* and *S. mirabilis* and is associated with subtropical water, mainly near shore sites; and Cluster 6 dominated by *I. aculeatum* belongs to sites from the Tasman Sea. Although these clusters are specific to the SW-Pacific, their biogeographic affinities may be taken into account, with certain consideration, when interpreting data from other Southern Hemisphere sites such as U1534.

Recent input by Thöle et al. (in prep) has extended the most recent existing compilation of dinocyst surface sediments from the Southern Ocean (Marret et al., 2019) to a total of 655 samples (dataset "sh_655" Thöle et al., in prep) and additionally provided a sub-dataset ("wsi_100") containing 100 samples to focus on ice-proximal sites. Cluster analysis based on *k*-means of the relative abundance of dinocyst species on both datasets has led to the proposal of a 9-clusters solution for the Southern Hemisphere and a 5-cluster solution focussing on the ice-proximal sites south of 60 °S. Since Site U1534 is located 53 °S and also warmer influence

is desired to be detected, this study mainly focusses on the comparison of the dinocyst assemblage with the 9 clusters for the Southern Hemisphere. Nevertheless, the 5 clusters for wsi_100 may still be considered for the glacial phase MIS 12.

The 9 clusters are characterized by one dominant dinocyst species, together with a variety of less abundant species and can be found in Thole et al. (in prep).

Appendix IV. Cross plot of various branched GDGT indices

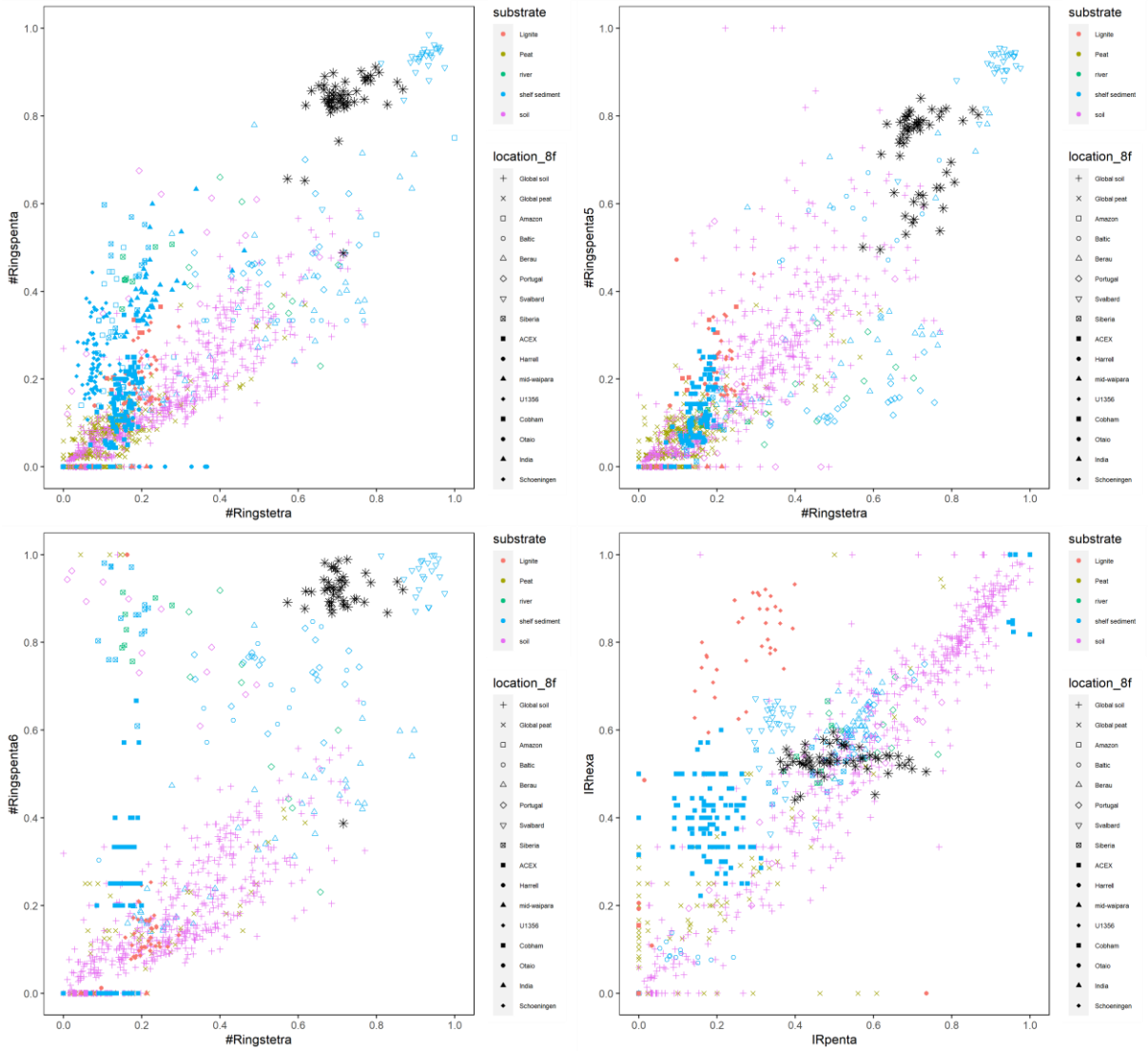

Upper left: #ringstetra vs. #ringspenta, Upper right: #ringstetra vs. #ringspenta5,
left below: #ringstetra vs. #ringspenta6, right below: IRpenta vs. IRhexa

Appendix V. MAAT and other brGDGT reconstructions

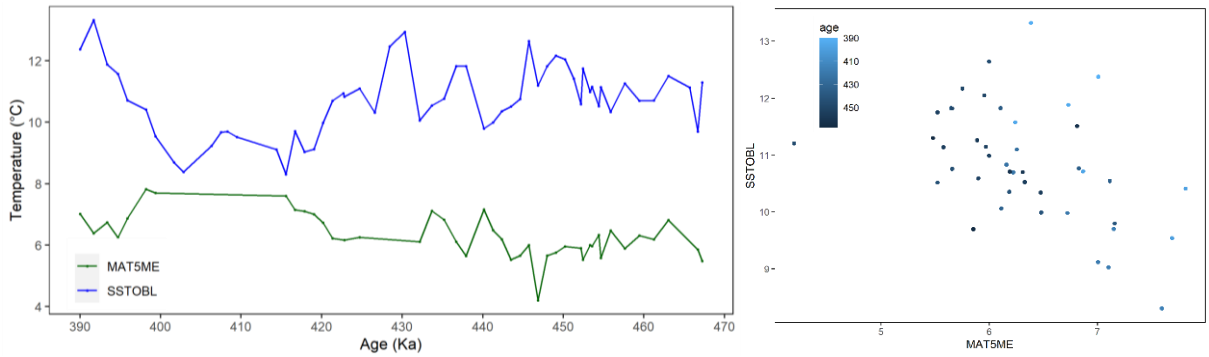

Figure 26. (left) BrGDGT-based MAAT reconstructions with the overprints removed; together with $SST_{lin}(TEX_{86})$ (O'Brien et al., 2017)**;** (right) Cross correlation between SST and MAAT.

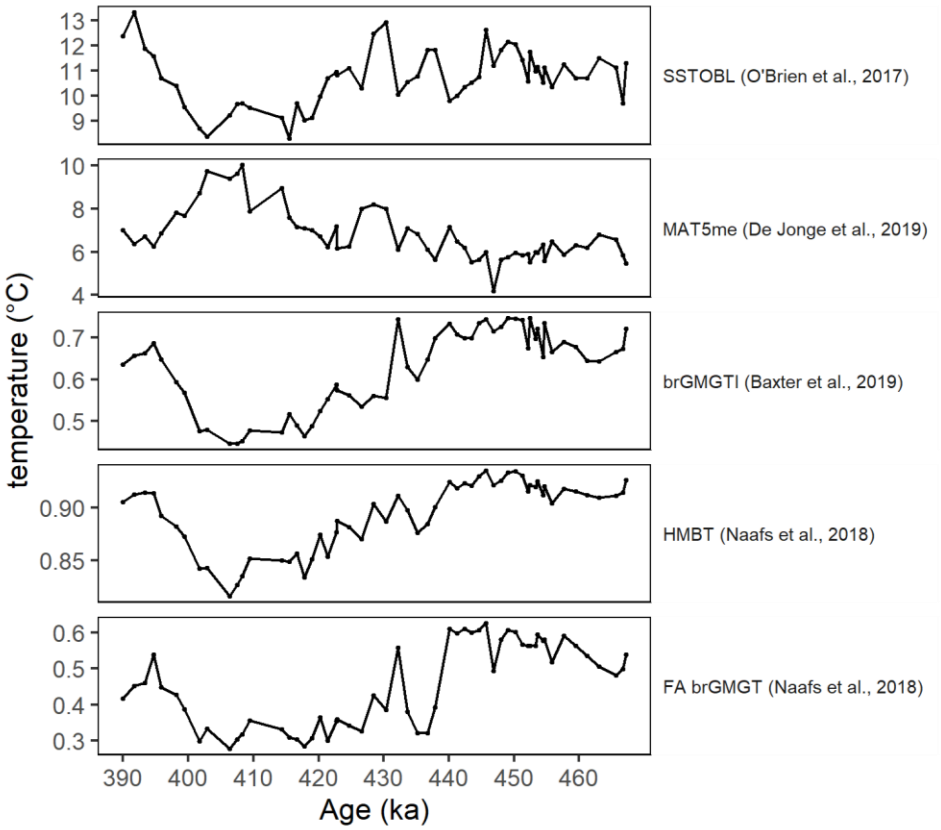

If no samples were discarded, MAAT air temperature displays atmospheric warming that started at ca. 448 ka, thus starting ~10 kyr before the glacial maximum of MIS 12. Air temperature rises to a maximum around ca. 405 ka and decreases again from ca. 405 ka onward. This pattern generally mirrors the SST record. The cross plot between TEX_{86}-based SST and MAAT does indeed not indicate any correlation at all.

Appendix VI. Total dinocyst assemblage U1534A

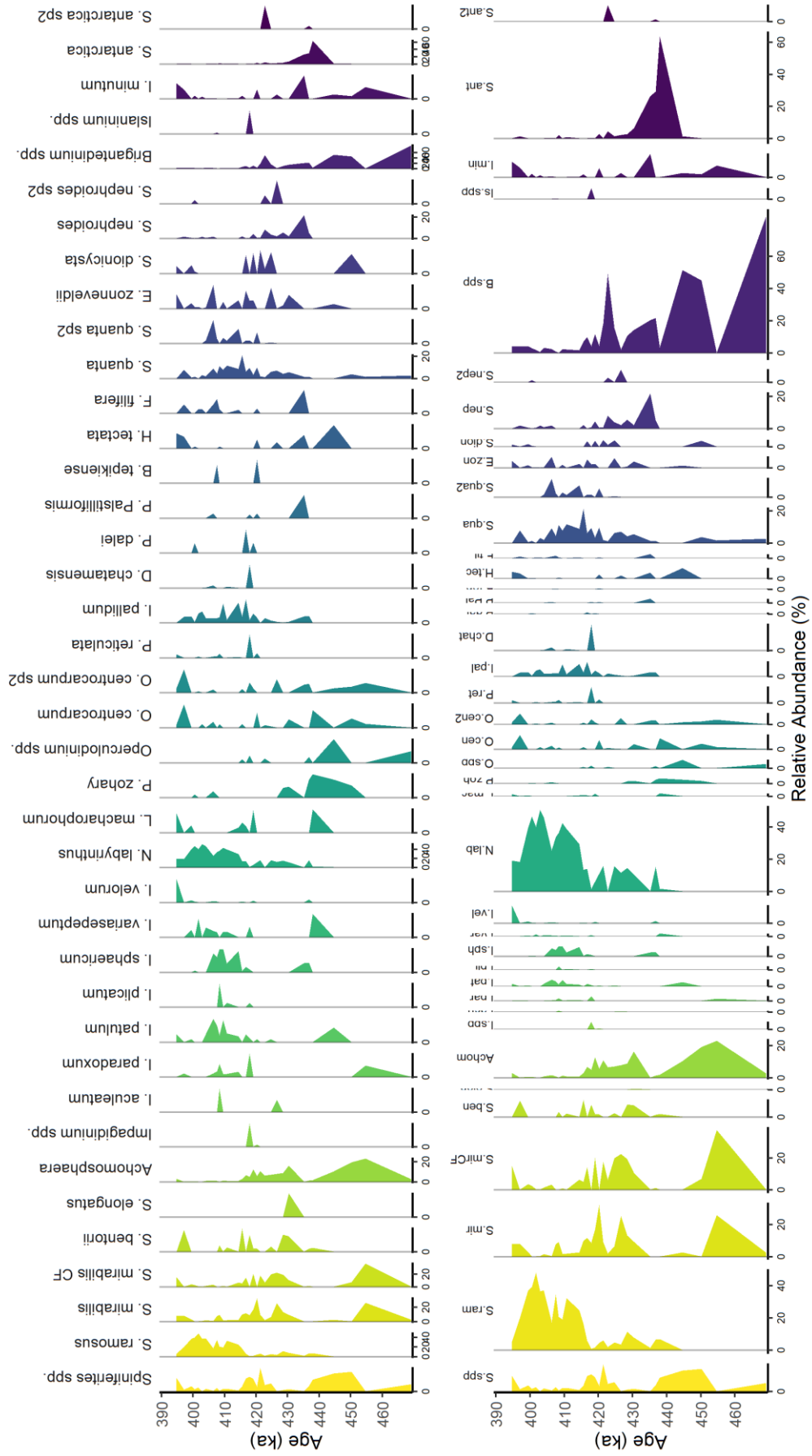

Appendix VII. Alternative plotting of dinocyst assemblage U1534

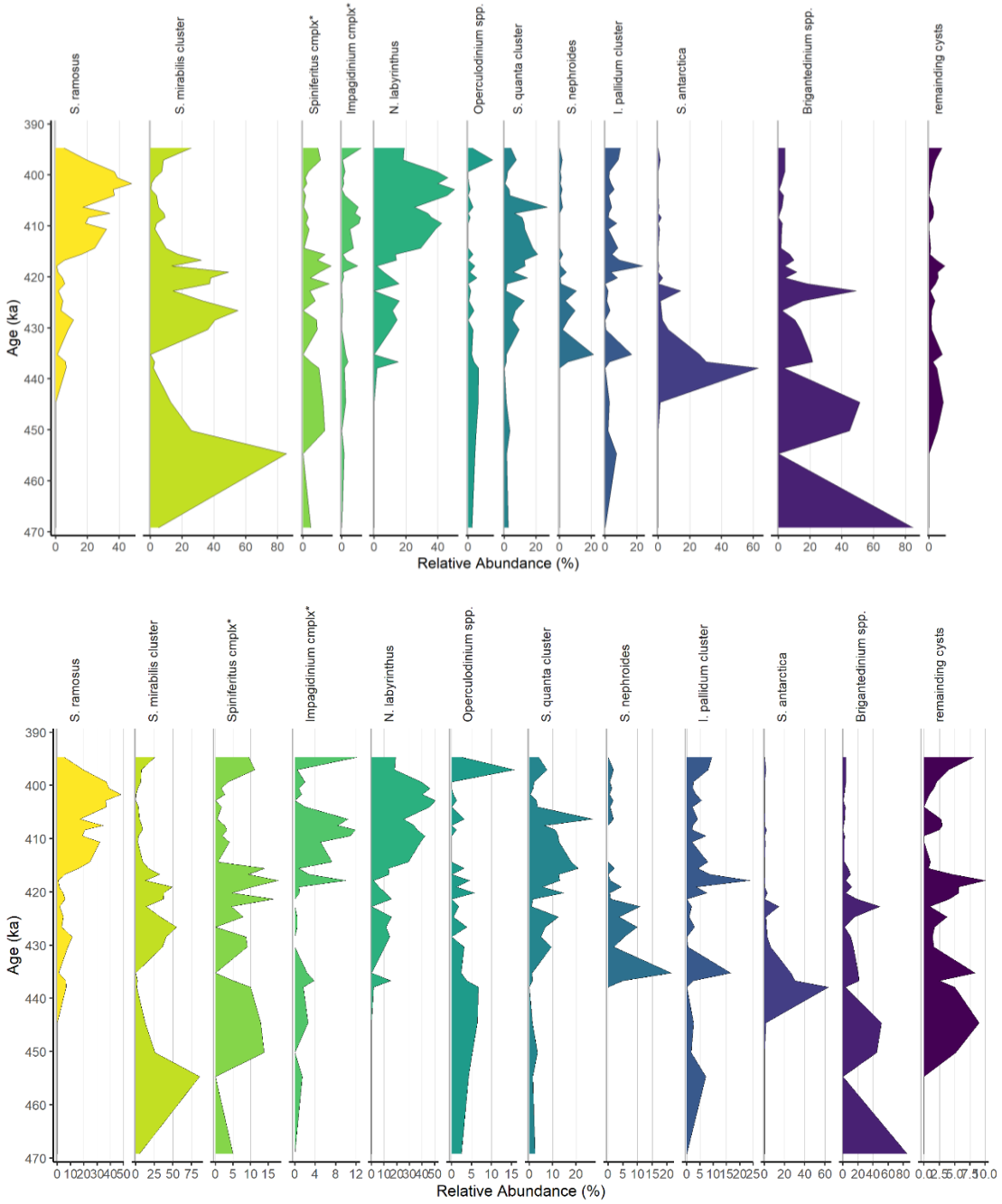

S. ramosus and *S. mirabilis* are plotted separate from the other *Spiniferites* spp. to indicate their individual distribution.